Title: **Polynomial filters for camera-based structural intensity analysis on curved plates.**

Authors: Felix Simeon Egner[a,b], Luca Sangiuliano[a,b], Régis Fabien Boukadia[a,b], Sjoerd van Ophem[a,b], Wim Desmet[a,b], Elke Deckers[b,c]

[a] KU Leuven, Department of Mechanical Engineering, Celestijnenlaan 300, Heverlee, Belgium

[b] Flanders Make@KU Leuven, Heverlee, Belgium

[c] KU Leuven, Department of Mechanical Engineering, Campus Diepenbeek Wetenschapspark 27, Diepenbeek, Belgium

Corresponding author: Felix Simeon Egner
felix.egner@kuleuven.be
KU Leuven, Department of Mechanical Engineering
Celestijnenlaan 300 – box 2420
3001 Heverlee, Belgium

Status: **Revision 2**

Abstract

Structural intensity can be used as a measure to detect energy sources, sinks, and transfer paths in solid structures. It provides a valuable design tool for vibro-acoustic problems next to modal analysis. However, it has been proven very challenging to determine structural intensity experimentally for the general case of curved plates. This is due to the requirement of an accurate measurement of the full 3D vibrational field and the computation of spatial gradients thereof.
The purpose of this paper is to propose a mesh-free, inherently smoothing, polynomial filtering approach and investigate its application for structural intensity analysis on curved plates based on a stereo camera measurement. Numerical studies are conducted to determine reasonable algorithm parameters (discretization, fitting radius, and the number of iterations) and their performance for different levels of uncertainty and various displacement fields. The results show that, depending on the uncertainty in the measurement, optimal values of the algorithm parameters exist. Furthermore, it is essential to achieve a high signal-to-noise ratio in the camera measurement. The computation of structural intensity is validated experimentally on the case of a flat plate and a curved plate (mockup oil pan). For the flat plate, good agreement with a reference finite element simulation is obtained. While it is not possible to derive quantitative results for the mockup oil pan under realistic measurement uncertainty, qualitative conclusions can be still drawn.

Keywords: structural intensity, stereo camera, experimental, polynomial filtering, curved plate

Nomenclature

$\bullet\vert_{\circ}$	$\bullet$ is represented in coordinates $\circ$
$\bullet^{*}$	Complex conjugate of $\bullet$
$\bullet_{\circ}$	Derivative of $\bullet$ with respect to $\circ$
$\dot{\bullet}$	Temporal derivative of $\bullet$
$\hat{\bullet}$	Estimation of $\bullet$
j	Imaginary unit
$\mathrm{Re}(\bullet)$	Real part of $\bullet$
$\tilde{\bullet}$	Projection of $\bullet$
DOF	Degree of freedom
FE	Finite element
MRE	Mean relative error
RE	Relative error
SI	Structural intensity
SLDV	Scanning Laser Doppler Vibrometry
SNR	Signal-to-noise ratio
α, β	Curvilinear coordinates
χ_i	Bending curvature
χ_{12}	Torsion
δ	Discretization
ϵ_i	Normal strain
ϵ_{12}	Shear strain
η	Structural damping
γ	Scale
κ_i	Curvature
ν	Poisson number
ρ	Density
θ_i	Rotation
$\mathbf{\Sigma}$	Covariance matrix
$\mathbf{d}$	Distance
$\mathbf{e}$	Unit vector
$\mathbf{I}$	Structural intensity vector
$\mathbf{P}$	Projection matrix
$\mathbf{R}$	Rotation matrix
$\mathbf{S}$	Shape operator
$\mathbf{s}$	Displacement vector
$\mathbf{s}^{h/2}$	Displacement vector at the outer surface
$\mathbf{w}$	Weights
$\mathbf{x}$	Point cloud
C	Extensional stiffness
c	Polynomial coefficients
D	Bending stiffness
E	Young's modulus
f	Frequency
h	Thickness
M_i	Bending moment
M_{12}	Twisting moment
N_i	Normal force
N_{12}	In-plane shear force
n_{c}	Number of points in the local neighborhood
n_{p}	Number of points
O^{123}	Principal coordinates
O^{uvw}	Fitting coordinates
O^{xyz}	World coordinates
p	2D polynomial
Q_i	Transverse shear force
r_{f}	Fitting radius
t	Time

1 Introduction

Acoustic intensity is a common measure for wave propagation in fluids. It is applied e.g. to locate acoustic sources and to assess radiated sound power or acoustic transmission loss. Equivalently, structural intensity (SI) can be used to analyze wave propagation in solid structures. In contrast to intensity probes for acoustic intensity, there is no direct measurement system available for SI. Instead, current approaches to measuring SI rely on a combination of full-field measurements, mechanical models, and constitutive equations. Previous studies have used mechanical models for beams [13], flat plates [2, 7, 18, 30], and limited examples of curved plates [11, 21]. Moreover, in practice, a SI analysis is possible even on solid bodies by considering the surface SI only, instead of the SI averaged over a cross section of the body [16, 25].

Amongst others, SI has been applied in the literature for transfer path analysis and source localization [1, 6, 15, 22, 23, 32], active control [27] and structural health monitoring [25]. The main challenge for the evaluation of SI is, apart from measuring the full vibrational field, that spatial gradients need to be computed. Specifically, spatial gradients up to the third order of the vibrational field (or even the fourth order for evaluation of the divergence) need to be computed and the process of numerical differentiation is considered unstable [17, 30]. Furthermore, for curved surfaces, the spatial gradients need to be computed along the surface. This requires knowledge about the geometry of the surface in the form of local, principal coordinate systems and surface derivatives [19].

There are several approaches to spatial gradient computation for SI analysis in the literature. In [7, 15, 20, 23] the spatial Fourier transform is applied for the task of numerical differentiation (*k-space* differentiation). The differentiation in *k-space* allows to efficiently filter high-wavenumber noise from the measurement through spatial filters. However, on the downside, the Fourier transform requires the measurement positions to be located on a regular grid and the vibrational field is implicitly assumed to be spatially periodic. Therefore, this approach is not suitable for the application to cases with increased geometrical complexity and unstructured measurement points.
Applied to flat plates, a global spline fit was used in [30] for the numerical differentiation. The authors note that the spline fit acts as a low-pass filter depending on the choice of knot positions and the degree of the spline. Furthermore, there is no restriction in terms of structured data or boundary conditions. In principle, a global spline can be fitted to complex surface geometries, however, there is a substantial risk of overfitting if know positions and degree of the spline are not selected carefully. This renders an automation of such a procedure difficult.
Classical finite differences were applied for numerical differentiation in [2] for a flat plate and in [11] for a curved plate. However, since a limited amount of measurement locations is used, the robustness against measurement noise is limited.
Another method for the numerical differentiation is the finite element (FE) approximation [1, 6, 18, 21, 32]. Thereby, the measured vibrational field is mapped onto an FE-mesh and FE-shape functions are used for the numerical differentiation. This approach has the advantage to be applicable for unstructured, 3D measurement data. Furthermore, through the global mapping onto shape functions, the smoothness of the vibrational field is enforced. However, the FE-approximation requires a suitable mesh and might be computationally expensive for large node numbers.

Apart from the method for numerical differentiation, different transducers have been used to measure the vibrational field required for SI analysis. In the following, only approaches resulting in 3D measurement data are considered. 3D Scanning Laser Doppler Vibrometry (SLDV) was used in [11, 32] to acquire the 3D components of the vibrational field. While producing very accurate measurement data, the drawback of 3D SLDV is the sequential scanning of measurement points (long measurement duration and restriction to steady-state phenomena) and its restrictively high costs. As an alternative measurement system, stereo cameras come to the fore. At the cost of increased measurement uncertainty and restrictions in frequency range, cameras offer the advantage of fast, inexpensive, and very dense 3D displacement measurements. They have been successfully applied for SI analysis in [21].

In this paper, the focus is on the general case of thin, curved plate-like structures (shells) including flat plates as a simplification. They occupy an important position in various fields of engineering, e.g. as parts of vehicles, machinery casings or containment structures. Assessing the SI flow through shells can provide valuable criteria to design their vibro-acoustic behavior. The analyzed structures are assumed to behave according to the general linear theory of shells, which allows reducing the dynamics of the shell to its 2D midsurface. Thereby, the Kirchhoff-Love assumptions need to be valid [29]. Furthermore, the material is assumed to be homogeneous, isotropic, and elastic.
Because of its smoothing abilities, mesh-free nature, and point-wise processing which is potentially suitable for parallelization, in this paper a method based on polynomial filters is proposed for the task of numerical differentiation. Specifically, polynomial filtering is extended from the well-known Savitzky-Golay filter [24] for 2D measurement data to be applicable to general shells and its use for SI analysis is investigated. It was shown in [3] that FE-approximation and polynomial filtering (named diffuse approximation) performed similarly in accuracy for the computation of gradients for stress evaluation based on the displacement field of a flat plate.
A stereo camera system is adopted for the measurement of the 3D vibrational field. Moreover, gradient-based Lucas-Kanade optical flow is employed to evaluate the displacement field from the image sequence. Thereby an equivalent procedure as described in [8] is used and will not be further elaborated on in this paper for compactness.
In summary, the contributions of the present paper are:

- Extension of the polynomial filtering approach to general shells
- Numerical study of the processing parameters for polynomial filtering
- Experimental investigation of the proposed approach for SI analysis on flat plates and curved plate-like structures

The paper is organized as follows. Section 2 introduces the theory of structural intensity in shells. The following section 3 describes the extension of the polynomial filtering approach and section 4 numerically investigates its properties and processing parameters. In section 5 polynomial filtering is applied for structural intensity analysis on a numerical case. Finally, section 6 presents experimental validation cases for a flat plate and a curved plate-like structure. Section 7 concludes the paper by summarizing the main findings.

2 Structural intensity

The theory for the SI computation in general shells is based on the work by Pires, Vanlanduit, and Dirckx in [19] which includes an extensive derivation of analytical equations expanding the required derivatives. For details on the general theory of shells, it is referred to the textbook [29]. In the following, a summary of the main relations involved in the computation of SI is given.

Intensity is defined as oriented, transferred power per unit area and can be computed as the product of a potential quantity and a flow quantity. In the structural domain, the potential quantity is the stress tensor and the flow quantity is the velocity vector. Specifically for shell structures surrounded by air as shown in fig. 1a, the component of the intensity in the thickness direction can be neglected since the energy exchange with the surrounding medium is small [17]. This results in an intensity vector constrained within the tangential plane to the midsurface of the shell. In a local coordinate system, aligned with the tangential plane (O^{123} in fig. 1b) the 2D SI vector per unit thickness is:

$$\mathbf{I}(t) = \begin{bmatrix} I_1 \\ I_2 \end{bmatrix} = - \begin{bmatrix} N_1 \dot{s}_1 + N_{12} \dot{s}_2 - M_1 \dot{\theta}_1 + M_{12} \dot{\theta}_2 + Q_1 \dot{s}_3 \\ N_2 \dot{s}_2 + N_{12} \dot{s}_1 + M_2 \dot{\theta}_2 - M_{12} \dot{\theta}_1 + Q_2 \dot{s}_3 \end{bmatrix}. \tag{1}$$

Equation (1) is the time domain description of the SI, with the time t. The potential quantities N_1

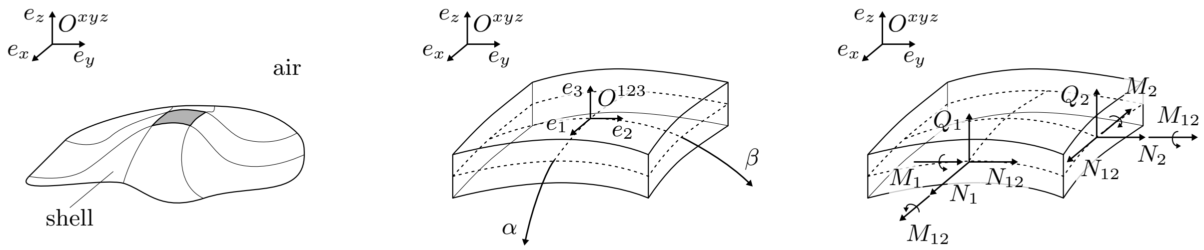

(a) General shell structure surrounded by air. Structural boundary conditions may apply to the lateral boundaries. O^{xyz} denotes the global coordinate system.

(b) Principal coordinate system in the midsurface of the shell (midsurface indicated by dashed lines).

(c) Internal forces and moments acting on the shell element (reaction forces and moments on the opposite side not indicated).

Figure 1: Shell model.

and N_2 are the normal forces, N_{12} is the in-plane shear force, M_1 and M_2 are the bending moments, M_{12} is the twisting moment and Q_1 and Q_2 are the transverse shear forces. Each potential quantity is multiplied with a flow quantity, i.e. the time derivative (denoted with the dot symbol) of the displacement s in the respective direction and the rotation θ around the respective axis. The internal forces and moments are schematically shown in fig. 1c. It should be noted that the minus sign in eq. (1) in front of M_1 and M_{12} arises from the definition of the rotation θ_1 in mathematical positive orientation (counterclockwise) and the overall minus sign is chosen to satisfy established stress conventions [16]. In the frequency domain, the instantaneous SI vector from eq. (1) is replaced by the steady state equation

$$\mathbf{I}(f) = \frac{1}{2}\,\mathrm{Re}\left(\mathrm{j}2\pi f \begin{bmatrix} N_1 s_1^* + N_{12} s_2^* - M_1\theta_1^* + M_{12}\theta_2^* + Q_1 s_3^* \\ N_2 s_2^* + N_{12} s_1^* + M_2\theta_2^* - M_{12}\theta_1^* + Q_2 s_3^* \end{bmatrix}\right). \tag{2}$$

The temporal derivative is converted to a multiplication with $\mathrm{j}2\pi f$ where j denotes the imaginary unit, f the frequency, and the star symbol denotes the complex conjugate. Taking the real part in eq. (2) indicates that active SI (the energy part that flows from source to sink) is considered while the imaginary part would result in the reactive SI (the energy part that purely oscillates between source and sink without producing a net flow) [11].

According to the Kirchhoff-Love plate theory, the internal forces and moments can be computed based on material properties (thickness h, Young's modulus E, density ρ, Poisson number ν and structural damping η) and gradients of the displacement field. Note that the gradients need to be evaluated along the surface, which results in additional terms as compared to regular volume gradients. A suitable coordinate frame for this computation are the principal coordinates [29]. They form an orthonormal coordinate system $[\mathbf{e}_1, \mathbf{e}_2, \mathbf{e}_3]$ and its first two base vectors are aligned with the direction of maximum curvature, κ_1 and minimum curvature κ_2 (denoted as α-direction and β-direction respectively, see fig. 1b) and the third base vector is aligned with the surface normal. Therefore, principal coordinates are a local property of the surface.

A camera measurement results in a displacement field (i.e. the measured vibrational field) at the surface of the plate-like structure, however, the Kirchhoff-Love plate theory makes use of relations in the midsurface of the shell. Thus, the measured displacement field at the outer surface $\mathbf{s}^{h/2}$ needs to be transformed to the midsurface:

$$\mathbf{s} = \begin{bmatrix} s_1 \\ s_2 \\ s_3 \end{bmatrix} = \begin{bmatrix} s_1^{h/2} - \frac{h}{2} s_{3,\alpha}^{h/2} \\ s_2^{h/2} - \frac{h}{2} s_{3,\beta}^{h/2} \\ s_3^{h/2} \end{bmatrix} \tag{3}$$

The notation subscripts α and β are used to denote gradients in principal coordinates along the surface. After transformation to the midsurface, the kinematic relations can be evaluated.

$$\theta_1 = s_1\kappa_1 - s_{3,\alpha} \qquad \theta_2 = s_2\kappa_2 - s_{3,\beta} \tag{4}$$
$$\epsilon_1 = s_{1,\alpha} + s_3\kappa_1 \qquad \epsilon_2 = s_{2,\beta} + s_3\kappa_2 \qquad \epsilon_{12} = s_{2,\alpha} + s_{1,\beta} \tag{5}$$
$$\chi_1 = -\theta_{1,\alpha} \qquad \chi_2 = \theta_{2,\beta} \qquad \chi_{12} = \theta_{2,\alpha} + s_{1,\beta}\kappa_1 \tag{6}$$

θ_1 and θ_2 are the rotations around the respective coordinate axis (in mathematical positive orientation), ϵ_1 and ϵ_2 are the normal strains, and ϵ_{12} is the shear strain. χ_1 and χ_2 are the bending curvatures and χ_{12} is the torsion of the surface. The derivatives of the kinematic relations in eqs. (4) to (6) can be derived analytically from derivatives of the displacement field up to the third order [19]. In combination with the material properties, the kinematic relations are used to derive the internal forces and moments acting on the surface:

$$M_1 = D(\chi_1 + \nu\chi_2) \qquad M_2 = D(\chi_2 + \nu\chi_1) \qquad M_{12} = M_{21} = D(1-\nu)\chi_{12} \tag{7}$$
$$N_1 = C(\epsilon_1 + \nu\epsilon_2) \qquad N_2 = C(\epsilon_2 + \nu\epsilon_1) \qquad N_{12} = N_{21} = C(1-\nu)\epsilon_{12} - M_{12}\kappa_2 \tag{8}$$
$$Q_1 = M_{12,\beta} + M_{1,\alpha} \qquad Q_2 = M_{12,\alpha} + M_{2,\beta}. \tag{9}$$

In eqs. (7) to (9) the extensional stiffness C and the bending stiffness D are defined as

$$C = \frac{Eh}{1-\nu^2} \qquad D = \frac{Eh^3}{12(1-\nu^2)}. \tag{10}$$

Eventually, the SI can be computed from eq. (1) (time domain) or eq. (2) (frequency domain). In this paper, the data will be processed in frequency domain to make use of temporal averaging for noise reduction.

3 Methods

The proposed polynomial filtering approach consists of two steps. First the geometry of the shell is approximated from the static point cloud by extending polynomial filtering to general shells. Local principal coordinate systems are estimated in every measurement point and curvature as well as higher-order derivatives of the surface are obtained. In a second step the spatial gradients of the displacement field are estimated by polynomial approximation in principal coordinates. As a result, all terms to evaluate the SI, eq. (2), are available. An outline of the polynomial filtering method is displayed in fig. 2.

3.1 Geometry approximation

The input for the geometry approximation is an unstructured point cloud $\mathbf{x} \in \mathbb{R}^{3\times n_\mathrm{p}}$ with n_p points, originating from the camera measurement. In a point-wise manner, 2D polynomial functions of third order are fitted to the point cloud (polynomial filter). Using the polynomial as proxy, surface gradients can be evaluated and subsequently principal coordinates computed from relations of differential geometry. Similar polynomial fitting approaches were reported in [14, 26] for the purpose of computing curvature and crease information from point clouds. However, in this paper fourth order polynomials are used to obtain all necessary gradients for SI evaluation. Moreover, the resulting surface information is further used to derive gradients of the vibrational field.
For the fit, the neighborhood consists of all n_c points $\mathbf{x}_\mathrm{c} \in \mathbb{R}^{3\times n_\mathrm{c}}$ within the fitting radius r_f to the current point as visualized in fig. 3a. The computations are equivalent for every point in the point cloud and for compactness of notation the index i indicating the current point $\mathbf{x}_i \in \mathbb{R}^{3\times 1}$ is omitted from now on whenever the local neighborhood is concerned.

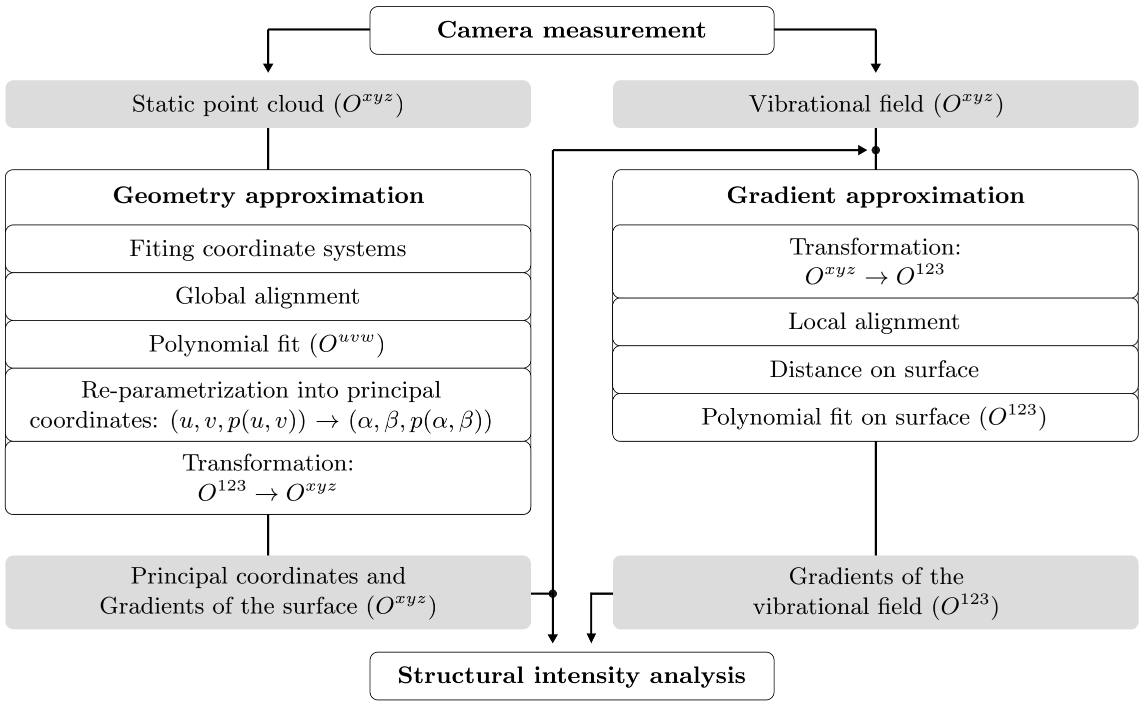

Figure 2: Outline of the polynomial filtering method.

Fitting coordinate system In the first step, an initial fitting coordinate system for performing the polynomial approximation is estimated from an implicit plane fit on the 3D point locations. The result is the tangential plane as indicated in fig. 3b. The purpose of the fitting frame is to provide a reasonable estimation of the surface-normal direction such that the subsequent polynomial fit is well-conditioned. For this task, the covariance matrix $\mathbf{\Sigma} \in \mathbb{R}^{3\times 3}$ is computed from the distances of the local neighborhood to the considered point $\mathbf{d} \in \mathbb{R}^{3\times n_\mathrm{c}} = \mathbf{x}_\mathrm{c} - \mathbf{x}_i$:

$$\mathbf{\Sigma} = \sum_{j=0}^{n_\mathrm{c}-1} \mathbf{w}_j \mathbf{d}_j \cdot \mathbf{d}_j^T. \tag{11}$$

Thereby, the index j goes over all points in the local neighborhood and the distances are weighted by a Gaussian weighting function [9]

$$\mathbf{w} \in \mathbb{R}^{1\times n_\mathrm{c}} = (d_\mathrm{max}\sqrt{2\pi})^{-1} e^{\frac{-|\mathbf{d}|^2}{2 d_\mathrm{max}^2}} \tag{12}$$

with $d_\mathrm{max} = \max(|\mathbf{d}|)$. The rotation matrix for the orthonormal fitting coordinate system (O^{uvw}), $\mathbf{R}_\mathrm{f} \in \mathbb{R}^{3\times 3} = [\mathbf{e}_\mathrm{u}, \mathbf{e}_\mathrm{v}, \mathbf{e}_\mathrm{w}]$, is subsequently obtained from the eigenvectors of the covariance matrix. The normal direction, $\mathbf{e}_\mathrm{w}$, is determined by the eigenvalue with the smallest magnitude. For consistency over the whole surface, the normal directions of the fitting coordinate systems are aligned according to the third principal direction of the whole point cloud. This works as long as the correct normal direction is not tilted by more than 90° from the third principal direction of the whole point cloud.

2D polynomial fit, principal coordinates, and surface gradients In the second step, the local neighborhood is approximated by a 2D polynomial of order n (fitted polynomial in fig. 3b). To this extend the local neighborhood is transformed into the fitting coordinate system $\mathbf{x}_\mathrm{c}|_\mathrm{f} = \mathbf{R}_\mathrm{f}^T(\mathbf{x}_\mathrm{c} - \mathbf{x}_i)$ (the vertical bar is used to denote "represented in a specific coordinate system"). In this representation

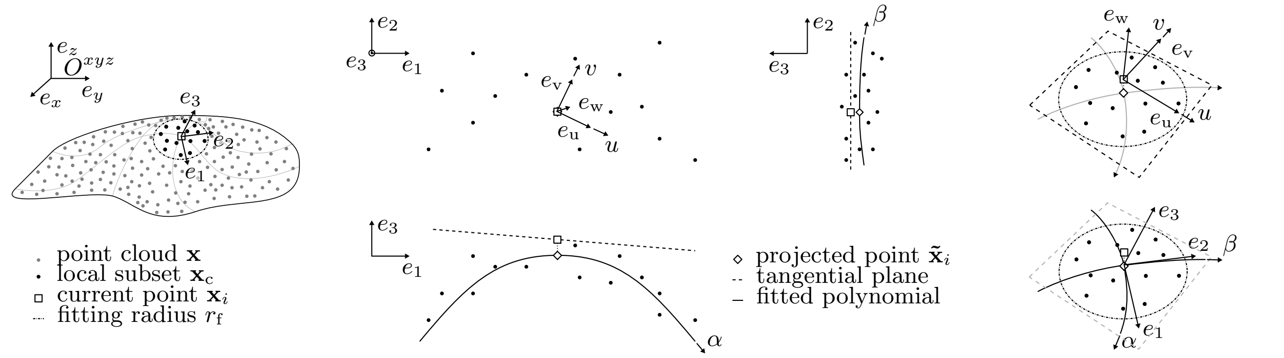

(a) Selection of the local neighborhood through the fitting radius.

(b) Fit of the tangential plane and polynomial approximation from the perspective of the principle coordinates.

(c) Transformation from fitting coordinates (top) to principal coordinates (bottom).

Figure 3: Geometry approximation.

the local neighborhood is approximated in a least squares sense by a 2D polynomial $p(u, v)$ with the base coordinates u and v and coefficients c_{jk}:

$$p(u, v) = \sum_{j=0}^{n_\mathrm{o}-1} \sum_{k=0}^{n_\mathrm{o}-j-1} c_{jk} u^j v^k. \tag{13}$$

A minimization yields the estimation of the polynomial coefficients,

$$\hat{c}_{jk} = \min_{c_{jk}} \sum_{l=0}^{n_\mathrm{c}-1} \left| p(x_{l,1}, x_{l,2}) - x_{l,3} \right|^2 . \tag{14}$$

Thereby, $x_{l,1/2/3}$ is the first/second/third coordinate of the lth point in the local neighborhood, in fitting coordinates, $\mathbf{x}_\mathrm{c}|_\mathrm{f}$. In 3D space the polynomial is represented as $\mathbf{p}(u, v) \in \mathbb{R}^{3\times1} = [u, v, p(u, v)]^T$ and it is parametrized as a function of the fitting coordinates. Since the current point, which in the fitting coordinate system is located at the origin, does not necessarily lie on the fitted polynomial, it is projected onto the polynomial along the surface normal, see fig. 3b. Practically, this is achieved by an iterative *Newton-Raphson* procedure, resulting in the projected point $\tilde{\mathbf{x}}_i|_\mathrm{f} = \mathbf{p}(\tilde{u}, \tilde{v})$.
The tangential space at the projected point is given by $\mathbf{p}_\mathrm{u}(\tilde{u}, \tilde{v})$ and $\mathbf{p}_\mathrm{v}(\tilde{u}, \tilde{v})$ with indices u and v indicating spatial derivatives in the directions of $\mathbf{e}_\mathrm{u}$ and $\mathbf{e}_\mathrm{v}$ respectively. Additionally, the normal vector is obtained as

$$\mathbf{e}_3 \in \mathbb{R}^{3\times1} = \frac{\mathbf{p}_\mathrm{u}(\tilde{u}, \tilde{v}) \times \mathbf{p}_\mathrm{v}(\tilde{u}, \tilde{v})}{|\mathbf{p}_\mathrm{u}(\tilde{u}, \tilde{v}) \times \mathbf{p}_\mathrm{v}(\tilde{u}, \tilde{v})|}. \tag{15}$$

The principal directions in the tangential plane, are then computed as the eigenvectors $\mathbf{e}_{\mathrm{S}1}$ and $\mathbf{e}_{\mathrm{S}2}$ of the shape operator of the surface [14]:

$$\mathbf{S} \in \mathbb{R}^{2\times2} = (EG - F^2)^{-1} \begin{bmatrix} LG - MF & ME - LF \\ ME - LF & NE - MF \end{bmatrix} \quad \text{with} \tag{16}$$

$$E = \mathbf{p}_\mathrm{u}(\tilde{u}, \tilde{v}) \cdot \mathbf{p}_\mathrm{u}(\tilde{u}, \tilde{v}) \qquad F = \mathbf{p}_\mathrm{u}(\tilde{u}, \tilde{v}) \cdot \mathbf{p}_\mathrm{v}(\tilde{u}, \tilde{v}) \qquad G = \mathbf{p}_\mathrm{v}(\tilde{u}, \tilde{v}) \cdot \mathbf{p}_\mathrm{v}(\tilde{u}, \tilde{v})$$
$$L = \mathbf{e}_3 \cdot \mathbf{p}_\mathrm{uu}(\tilde{u}, \tilde{v}) \qquad M = \mathbf{e}_3 \cdot \mathbf{p}_\mathrm{uv}(\tilde{u}, \tilde{v}) \qquad N = \mathbf{e}_3 \cdot \mathbf{p}_\mathrm{vv}(\tilde{u}, \tilde{v})$$

A projection with $\mathbf{P} \in \mathbb{R}^{3\times2} = [\frac{\mathbf{p}_\mathrm{u}(\tilde{u},\tilde{v})}{|\mathbf{p}_\mathrm{u}(\tilde{u},\tilde{v})|}, \frac{\mathbf{p}_\mathrm{v}(\tilde{u},\tilde{v})}{|\mathbf{p}_\mathrm{v}(\tilde{u},\tilde{v})|}]$ yields the principal directions $\mathbf{e}_1 \in \mathbb{R}^{3\times1} = \mathbf{P}\mathbf{e}_{\mathrm{S}1}$ and $\mathbf{e}_2 \in \mathbb{R}^{3\times1} = \mathbf{P}\mathbf{e}_{\mathrm{S}2}$ in 3D space. The local, orthonormal principal coordinate system is defined through

the rotation matrix $\mathbf{R}_\mathrm{p}|_\mathrm{f} \in \mathbb{R}^{3\times3} = [\mathbf{e}_1, \mathbf{e}_2, \mathbf{e}_3]$, see fig. 3c. For subsequent computations the principal coordinates are transformed back to the global coordinate system with $\mathbf{R}_\mathrm{p} = \mathbf{R}_\mathrm{f}\mathbf{R}_\mathrm{p}|_\mathrm{f}$. Furthermore, transformation of the projected current point yields a smoothed point cloud: $\hat{\mathbf{x}}_i = \mathbf{R}_\mathrm{f}\tilde{\mathbf{x}}_i|_\mathrm{f} + \mathbf{x}_i$.
To evaluate the gradients of the surface in principal directions, the fitted polynomial is re-parametrized as a function of the principal coordinates α and β. Centering the polynomial around the projected point and applying the principal rotation yields the following transformation:

$$\begin{bmatrix} u(\alpha,\beta) \\ v(\alpha,\beta) \end{bmatrix} = [\mathbf{e}_{S1}, \mathbf{e}_{S2}]^T \begin{bmatrix} \alpha \\ \beta \end{bmatrix} - \begin{bmatrix} \tilde{u} \\ \tilde{v} \end{bmatrix}. \tag{17}$$

Insertion into the fitted polynomial, eq. (13), allows to analytically determine the gradients in principal directions.
Since the principal directions lie in the tangential plane to the surface, the first-order gradients vanish, $p_\alpha = 0$ and $p_\beta = 0$. The second-order single direction gradients are equal to the maximal and minimal curvature, $p_{\alpha\alpha} = \kappa_1$ and $p_{\beta\beta} = \kappa_2$, and the second-order cross gradients vanish as well, $p_{\alpha\beta} = p_{\beta\alpha} = 0$. In general, the third- and possible higher-order derivatives are non-zero. Algorithm 1 shows the complete procedure for the geometry approximation is summarized in pseudocode.

Algorithm 1 Geometry approximation

procedure GEOMETRY_APPROXIMATION($\mathbf{x}$, r_f)
  for i in range(n_p) **do**
    $\mathbf{x}_{\mathrm{c},i} \leftarrow \mathbf{x}_j$ if $|\mathbf{x}_j - \mathbf{x}_i| < r_\mathrm{f}$
    $\mathbf{R}_{\mathrm{f},i} \leftarrow$ FITTING_COORDINATE_SYSTEM($\mathbf{x}_{\mathrm{c},i}$)
  end for
  $\mathbf{R}_\mathrm{f} \leftarrow$ ALIGN_COORDINATE_SYSTEMS($\mathbf{R}_\mathrm{f}$)
  for i in range(n_p) **do**
    $\mathbf{x}_{\mathrm{c},i}|_\mathrm{f} \leftarrow \mathbf{R}_{\mathrm{f},i}^T(\mathbf{x}_{\mathrm{c},i} - \mathbf{x}_i)$
    $\mathbf{p}_i \leftarrow$ FIT_POLYNOMIAL($\mathbf{x}_{\mathrm{c},i}|_\mathrm{f}$, n)
    $\tilde{\mathbf{x}}_i|_\mathrm{f} \leftarrow$ PROJECT_POINT($\mathbf{p}_i$, $\mathbf{x}_i|_\mathrm{f}$)
    $\mathbf{n}_i \leftarrow$ NORMAL_DIRECTION($\mathbf{p}_i$, $\tilde{\mathbf{x}}_i|_\mathrm{f}$)
    $\mathbf{R}_{\mathrm{p},i}|_\mathrm{f} \leftarrow$ PRINCIPAL_DIRECTION($\mathbf{p}_i$, $\tilde{\mathbf{x}}_i|_\mathrm{f}$)
    $\mathbf{R}_{\mathrm{p},i} \leftarrow \mathbf{R}_{\mathrm{f},i}\mathbf{R}_{\mathrm{p},i}|_\mathrm{f}$
    $\hat{\mathbf{x}}_i \leftarrow \mathbf{R}_{\mathrm{f},i}\tilde{\mathbf{x}}_i|_\mathrm{f} + \mathbf{x}_i$
    $p_{\alpha,\beta} \leftarrow$ EVALUATE_GRADIENTS_PRINCIPAL($\mathbf{p}_i$, $\tilde{\mathbf{x}}_i|_\mathrm{f}$, $\mathbf{R}_{\mathrm{p},i}|_\mathrm{f}$)
  end for
  return $\hat{\mathbf{x}}$, $\mathbf{R}_\mathrm{p}$, $p_{\alpha,\beta}$
end procedure

3.2 Gradient approximation

A strategy similar to the geometry approximation is proposed for the computation of the spatial gradients of the displacement field. In a point-wise procedure, all three components of the field are approximated by a 2D polynomial fit in local principal coordinates. Subsequently the fitted polynomials serve as a proxy for evaluating the required derivatives for SI computation.
The displacement field in the local neighborhood around the current point is denoted as $\mathbf{s}_\mathrm{c} \in \mathbb{C}^{3\times n_\mathrm{c}}$. It is transformed into local principal coordinates by

$$\mathbf{s}_\mathrm{c}|_\mathrm{p} = \tilde{\mathbf{R}}_{\mathrm{p},c}^T \mathbf{s}_\mathrm{c} \tag{18}$$

Note that the displacement field is transformed according to the principal coordinates corresponding to its base point, i.e. the transformation is different for each point. For a successful fit, it is essential

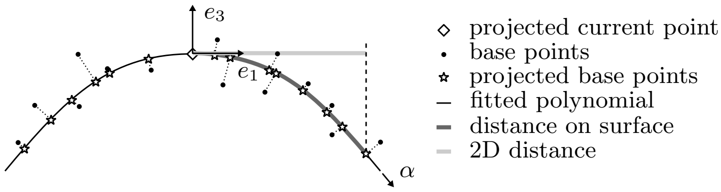

Figure 4: Projection onto the fitted polynomial and comparison of distance on the surface and 2D distance.

to avoid inconsistent orientations of the principal coordinates (they are only defined up to sign or arbitrary in the case of a flat surface). Since a global alignment of the principal directions is not generally feasible for a complex surface an alignment step constrained to the local neighborhood is performed: The first principal directions are aligned with the one of the current point through a rotation around the respective normal direction. This alignment results in aligned principal coordinates in the local neighborhood, represented through the rotation matrices $\tilde{\mathbf{R}}_{\mathrm{p},c}$.

To compute the derivatives along the surface, the distance of the base points for the fit is evaluated on the surface. This is in contrast to ordinary spatial derivatives in a volume, where the distance of the base points is equivalent to the distance in global coordinates, see fig. 4. For each point in the local neighborhood, the distance on the surface to the current point is evaluated from the previously fitted polynomial of the geometry approximation step. Since the measured points do not lie on the polynomial, a normal projection is performed to obtain the base points (*Newton-Raphson* procedure). The distance on the polynomial is evaluated through discretization into 100 line segments and yields the distance vector $\tilde{\mathbf{d}}$. Taking these distances into account, each component k of the displacement in the local neighborhood, $\mathbf{s}_{k,\mathrm{c}}|_{\mathrm{p}}$ is approximated by a polynomial:

$$\hat{c}_{jk} = \min_{c_{jk}} \sum_{l=0}^{n_{\mathrm{c}}-1} \left| p(\tilde{d}_{l,1}, \tilde{d}_{l,2}) - s_{l,k} \right|^2 . \tag{19}$$

Thereby, $\tilde{d}_{l,1/2}$ is the first/second component of the distance and $s_{l,k}$ is the kth displacement component in principal coordinates at the lth point of the local neighborhood.
Evaluation of the polynomial at the origin results in a smoothed displacement field $\hat{\mathbf{s}}|_{\mathrm{p}}$ as well as estimations of the spatial gradients in principal coordinates: $\hat{\mathbf{s}}_{\alpha}|_{\mathrm{p}}$ and $\hat{\mathbf{s}}_{\beta}|_{\mathrm{p}}$. Index α and β indicate derivatives in the respective direction of the local principal coordinates. The maximum order of the derivatives is dependent on the order of the fitted polynomial. This way, both single direction, as well as cross derivatives, can be evaluated. In algorithm 2 the procedure for the gradient approximation is summarized in pseudocode.

Algorithm 2 Gradient approximation

procedure GRADIENT_APPROXIMATION($\mathbf{x}$, r_f, $\mathbf{R}_\mathrm{p}$, $\hat{c}_{jk}$)
  for i in range(n_p) **do**
    $\mathbf{x}_\mathrm{c} \leftarrow \mathbf{x}_j$ if $|\mathbf{x}_j - \mathbf{x}_i| < r_\mathrm{f}$
    $\mathbf{s}_\mathrm{c} \leftarrow \mathbf{s}_j$ if $|\mathbf{x}_j - \mathbf{x}_i| < r_\mathrm{f}$
    $\mathbf{R}_{\mathrm{p,c}} \leftarrow \mathbf{R}_{\mathrm{p},j}$ if $|\mathbf{x}_j - \mathbf{x}_i| < r_\mathrm{f}$
    $\tilde{\mathbf{R}}_{\mathrm{p,c}} \leftarrow$ ALIGN_COORDINATE_SYSTEMS($\mathbf{R}_{\mathrm{p,c}}$)
    $\mathbf{s}_\mathrm{c}|_\mathrm{p} = \tilde{\mathbf{R}}^T_{\mathrm{p},c}\mathbf{s}_\mathrm{c}$
    $\tilde{\mathbf{d}} \leftarrow$ EVALUATE_DISTANCE_ALONG_SURFACE($\hat{c}_{jk}$, $\mathbf{x}_\mathrm{c}$)
    for k in range(3) **do**
      $\hat{\mathbf{s}}|_\mathrm{p}$, $\hat{\mathbf{s}}_{k,i,\alpha}|_\mathrm{p}$, $\hat{\mathbf{s}}_{k,i,\beta}|_\mathrm{p} \leftarrow$ FIT_POLYNOMIAL($\mathbf{s}_{k,\mathrm{c}}|_\mathrm{p}$, $\tilde{\mathbf{d}}$)
    end for
  end for
  return $\hat{\mathbf{s}}|_\mathrm{p}$, $\hat{\mathbf{s}}_\alpha|_\mathrm{p}$, $\hat{\mathbf{s}}_\beta|_\mathrm{p}$
end procedure

4 Numerical validation of the polynomial filtering method

This section investigates the proposed polynomial filtering method for geometry and gradient approximation numerically. To this extend the case of a cylinder with simulated measurement uncertainty is considered. The cylinder is parametrized with a unit curvature of $\kappa_1 = 1$, its diameter is $\frac{2}{\kappa_1}$ and its height is $\pi\frac{2}{\kappa_1}$. An equidistant grid of n_p points is created on a half of the cylinder surface leading to a discretization (unit distance) of $\delta = \frac{\pi}{\kappa_1(\sqrt{n_\mathrm{p}}-1)}$. Together, the curvature and the discretization determine the scale of the problem: $\gamma = \delta\kappa_1$. For constant scale, equivalent fitting problems are obtained. All subsequent results need to be interpreted relative to the scale. This indicates that for surfaces with higher curvature more points are required per length to obtain the same results.

4.1 Geometry approximation

The effects of the parameters measurement uncertainty, discretization, fitting radius, and the number of iterations are tested. Thereby, the measurement uncertainty is assumed to be zero-mean Gaussian noise and is applied to each point in surface normal direction. The fitting radius determines the number of points included in the point-wise approximation and is given in multiples of the discretization size. Since the geometry approximation produces a smoothed point cloud the effects of iterating the approximation procedure is investigated which is indicated by the iterations parameter.
As a single number metric for the algorithm performance the mean relative error of the estimated curvature is employed

$$\mathrm{MRE} = \mathrm{mean}\left(\frac{|\hat{\boldsymbol{\kappa}}_1 - \boldsymbol{\kappa}_1|}{|\boldsymbol{\kappa}_1|}\right) \cdot 100\,\%, \tag{20}$$

with $\boldsymbol{\kappa}_1$ the vector of curvature estimates for each point. Other error measures such as the normal distance between true and estimated points or other surface gradients could be used as well but the expectation is that the trend is similar since these quantities are dependent on each other. Generally, the error can be split into two contributions, the approximation error and the random error [3]. The approximation error is the bias of the approximation method and the random error is originating from the noise in the measurement.
The base case consists of a discretization with 900 points, a measurement uncertainty of $1 \cdot 10^{-4}$, a fitting radius of 6 multiples of unit distance and a single iteration. Since often the measurement uncertainty is not precisely known and is influenced by many factors it was chosen to overestimate this parameter for the base case (see [4] for detailed bias and uncertainty derivations and dependencies).

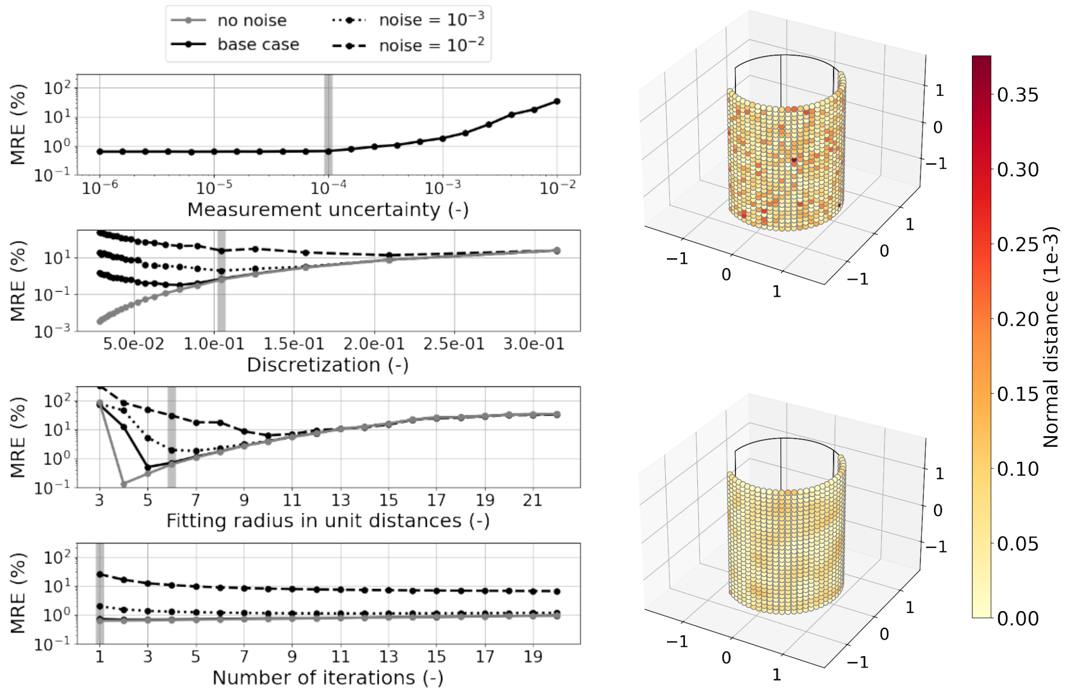

(a) Mean relative error of the curvature estimation for different parameter settings. The parameters for the base case are highlighted by the vertical gray bar.

(b) Spatial distribution of the normal distance for the base case. Points before approximation (top) and after approximation (bottom).

Figure 5: Numerical case: cylinder with uncertainty.

The results show that the MRE of the curvature is strongly dependent on the measurement uncertainty with an increased measurement uncertainty leading to an increased MRE (fig. 5a, top plot). However, the base case results in a MRE below 1 %. The approximation error (plotted in gray, no noise) decreases steadily with smaller discretization size (fig. 5a, second plot). However, for the cases with noise, an optimal discretization and subsequently and optimal scale exists from where a finer discretization again leads to a higher MRE. For example in the base case, a discretization $\delta = 0.08$ is optimal. The increase in MRE with finer discretization is attributed to the random error and is dependent on the amount of noise. With increasing noise levels the optimal scale increases, i.e. a larger part of the surface needs to be covered by the fitting radius.

Furthermore, there exists an optimal value of the fitting radius depending on the amount of noise (fig. 5a, third plot). This is a typical trade-off between underfitting (smoothing the data too severely, i.e. a large fitting radius) and overfitting (fitting the noise, i.e. a small fitting radius). While in the base case a fitting radius of 5 times the discretization size performs best, the optimal fitting radius increases with the amount of noise. The result is that a larger part of the surface and thus more points are covered by the fitting radius. Finally, performing multiple iterations reduces the MRE in case noise is present in the data (fig. 5a, bottom plot). Contrarily, multiple iterations are not beneficial in the case without noise which leads to the conclusion that iterating the approximation procedure reduces the random error only.

For the base case, the spatial distribution of the normal distance to the true points is shown in fig. 5b before and after approximation. It can be observed that the normal distance is reduced and the distribution is smoothed as a better approximation of the measurement data is obtained. This is true equivalently in the center as well as at the borders of the cylinder domain.

For the practical application of polynomial filtering, it is essential to select proper algorithm parameters. Therefore, the measurement uncertainty needs to be determined. Based on this, optimal settings for discretization, fitting radius and number of iterations can be selected from the results of the numerical study and the curvature (which determines the scale). Instead of adapting the parameters locally according to the local curvature, it is suggested to base the selection on the maximum curvature of the component for simplicity.

4.2 Gradient approximation

To study the properties of polynomial filtering for gradient approximation a harmonic displacement field is chosen as representative of a typical measurement of a vibrating surface. The displacement field is applied to the cylinder geometry and it is defined as:

$$s(\alpha, \beta) = A \sin(k^{\alpha}\pi\alpha)\sin(k^{\beta}\pi\beta). \tag{21}$$

The displacement field is parametrized by the principal coordinates (circumferential: α, vertical: β), the amplitude A, and the wavenumber k in the respective coordinate direction. In addition to the parameters of the displacement field, the same geometry parameters as in section 4.1 are varied in the parametric study. Instead of applying measurement uncertainty to the point location, the noise is applied to the displacement field. As an error measure, the relative error of the estimated field is applied

$$\mathrm{RE} = \frac{|\hat{\mathbf{s}} - \mathbf{s}|}{\max(|\mathbf{s}|)} \cdot 100\,\%, \tag{22}$$

where $\mathbf{s}$ can be the displacement field or the respective gradients. Because the gradients are expected to have zeros crossings the RE is computed relative to the maximum amplitude of the respective field instead of relative to the local amplitude at each point.
The base case parameters for the displacement field are a signal-to-noise ratio (SNR) of 40 dB and wavenumbers of 0.5 in both directions. The other base case parameters are equivalent to the study in section 4.1.

The true and the approximated gradients up to third order are shown in fig. 6 for the base case. For the visualization the fields were evaluated along the vertical coordinate in the middle of the cylinder. A qualitatively consistent approximation is visible for all gradient fields. It can be observed that the RE tends to be increased at the border of the domain (especially for second and third-order gradients). The reason is that at the border fewer and additionally non-symmetric points are available for the computation [31]. Well-known techniques like the usage of ghost points could be applied to reduce the error at the border but this is out of scope in the current study. Furthermore, the RE is increasing with increasing gradient order. This is also visible in fig. 7 where the RE was aggregated into the MRE by averaging over all points. For the spatial averaging, the borders of the domain were excluded up to the fitting radius to discard the influence of the missing points. Figure 7 shows that the MRE is approximately equal for gradients in both coordinate directions, there is no clear influence of the curvature. The MRE for first order gradients is below 0.1 %, for second order gradients below 3 % and for third order gradients below 6.5 %. While the second-order cross gradient ($s_{\alpha\beta}$) shows a slightly larger error than the second order single direction gradients ($s_{\alpha\alpha}$, $s_{\beta\beta}$), the error of the third-order cross gradients ($s_{\alpha\alpha\beta}$, $s_{\alpha\beta\beta}$) is lower than the third-order single direction gradients ($s_{\alpha\alpha\alpha}$, $s_{\beta\beta\beta}$). There is no clear dependency of the MRE on the gradient type but rather it is dependent on the order of the gradient.

For the parametric study, the spatial MRE was further aggregated by averaging over the gradient order to arrive at a single number metric suitable for comparison. The following results are therefore indicating a trend but the magnitude of the error will depend on the order of the gradients. As shown in fig. 8 the results are similar to the findings in section 4.1 for the geometry approximation. Again, the MRE is strongly related to the SNR (fig. 8a, top plot). A finer discretization decreases the

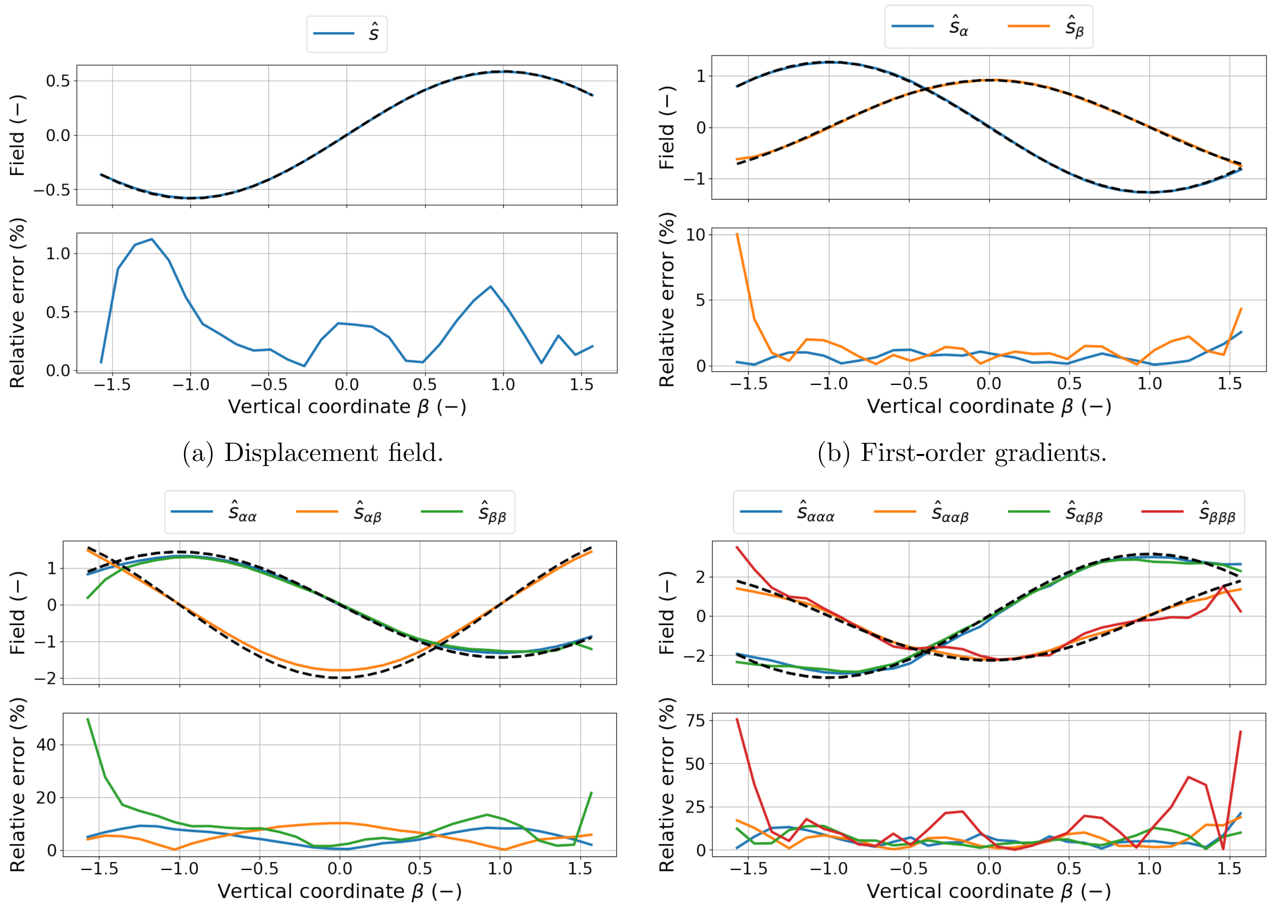

(a) Displacement field.

(b) First-order gradients.

(c) Second-order gradients.

(d) Third-order gradients.

Figure 6: Comparison of true (dashed black lines) and approximated (colored solid lines) displacement and gradient fields. The fields were evaluated in the middle of the cylinder geometry, along the vertical coordinate.

approximation error but when a random error is introduced through the noise in the measurement an optimal discretization and subsequently optimal scale exists (fig. 8a, second plot). Equivalent to the geometry approximation study a discretization of $\delta = 0.08$ is optimal in the base case. Depending on the noise level a larger fitting radius, as well as multiple iterations, are beneficial (fig. 8a, third and bottom plot). For the gradient approximation the minimal MRE is found with 6 times the discretization size at larger fitting radii than for the geometry approximation. The amplitude of the displacement field is irrelevant for the approximation error (no noise) but inversely correlates to the random error for constant noise levels (fig. 8b, top plot). Finally, the approximation error tends to increase with increasing wavenumber (fig. 8b, middle and bottom plot). The behavior is very similar for wavenumbers in both directions. It can be interpreted in the sense that the more complex the displacement field to approximate, the higher the MRE.

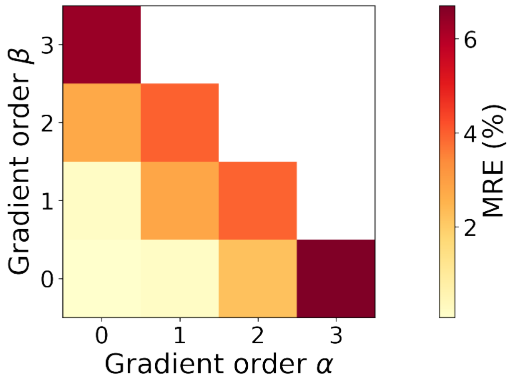

Figure 7: Comparison of spatial mean MRE for all gradient orders.

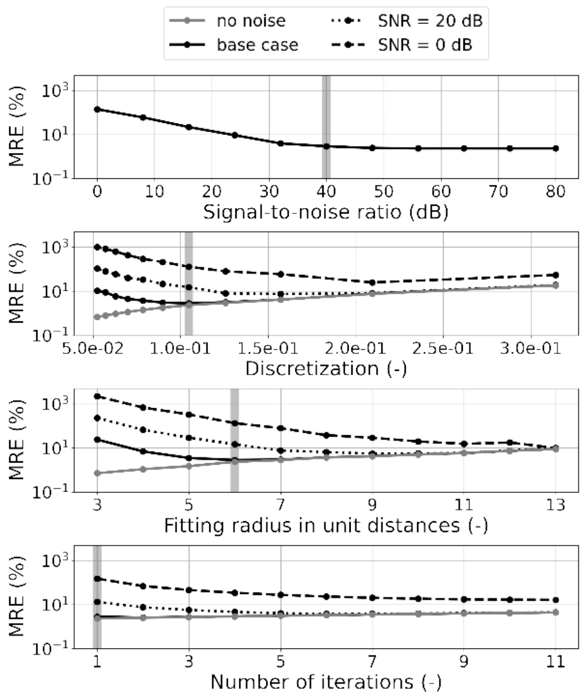

(a) Mean relative error of the gradient estimation for different parameter settings related to the geometry.

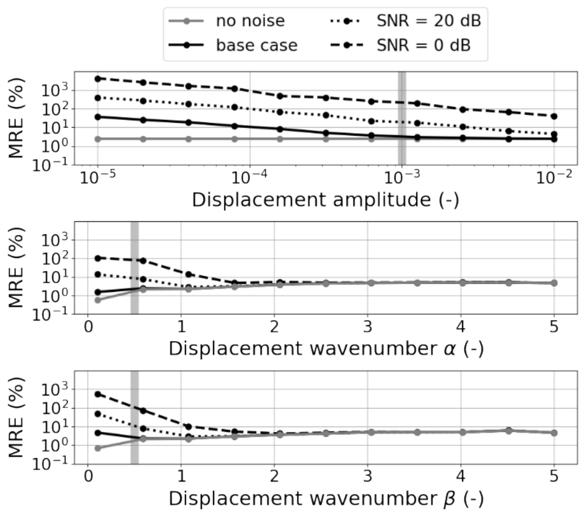

(b) Mean relative error of the gradient estimation for different parameter settings related to the displacement field.

Figure 8: Numerical case: harmonic displacement field with uncertainty on cylinder geometry. The parameters for the base case are highlighted by the vertical gray bar.

5 Numerical validation of the structural intensity analysis

This section numerically investigates polynomial filtering in combination with camera measurements for SI analysis of curved plate-like structures. The case of a curved plate-like structure (mockup oil pan), excited by a point force, is considered. First, the component is analyzed without taking measurement noise into account to validate the algorithm. Subsequently, the effect of measurement noise is studied.

5.1 Mockup oil pan excited by point force

The oil pan has a complex-shaped surface with various regions of different curvatures as well as flat panels. In industrial applications, the oil pan is known to be a source of acoustic radiation through its large flat panels [5, 10, 12]. In practice, SI analysis could be used to design the energy flow to avoid the vibration of these panels.

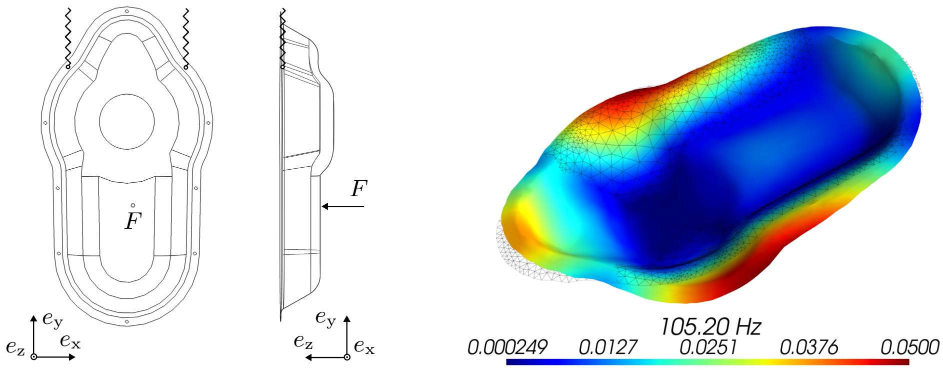

(a) Geometry of the component and location of the point force.

(b) Amplitude of the second mode shape of the component.

Figure 9: Oil pan example case.

The oil pan has dimensions of 0.85 m (length) by 0.46 m (width) by 0.14 m (height). It is subject to free-free boundary conditions and excited by a point force, see fig. 9. The excitation frequency is selected to be close to the second mode shape of the component, where large vibration amplitudes are expected. Since there is no energy sink present, the expectation is to observe circular SI flows within the structure and energy dissipation though internal losses.

For the analysis the component's parameters are assumed to be homogeneous (thickness of 1.7 mm, Young's modulus of $217 \cdot 10^9$ Pa, density of $7850\,\mathrm{kg/m^3}$, Poisson number of 0.3 and structural damping of 0.001.). The point cloud is generated by a reference FE-simulation which is also used as a benchmark for the SI evaluation. Shell elements with 6 degrees of freedom (DOF) per node (3 translation and 3 rotation) are used to model the component. The discretization size is 3 mm leading to a total of 305 466 DOFs or 50 911 nodes forming the point cloud.

With a maximum curvature of $|\kappa_1| = 75$ the maximum scale of the example case is $\gamma = 0.225$. Since no measurement uncertainty is applied, the scale is larger than the optimal value from section 4.1 and section 4.2. This is chosen deliberately to examine the robustness of the overall SI computation with respect to the discretization.

For the geometry approximation and the gradient approximation a fitting radius of 4 times the discretization size is selected. The resulting principal coordinates, as well as principal curvatures, are visualized in fig. 10 and fig. 11. It is observed that the first principal direction (red arrow in fig. 10) is consistently aligned with the direction of maximum curvature and regions of constant curvature are visible as such. Regarding the first principal curvature, fig. 11a, slight deviations are visible as wavy

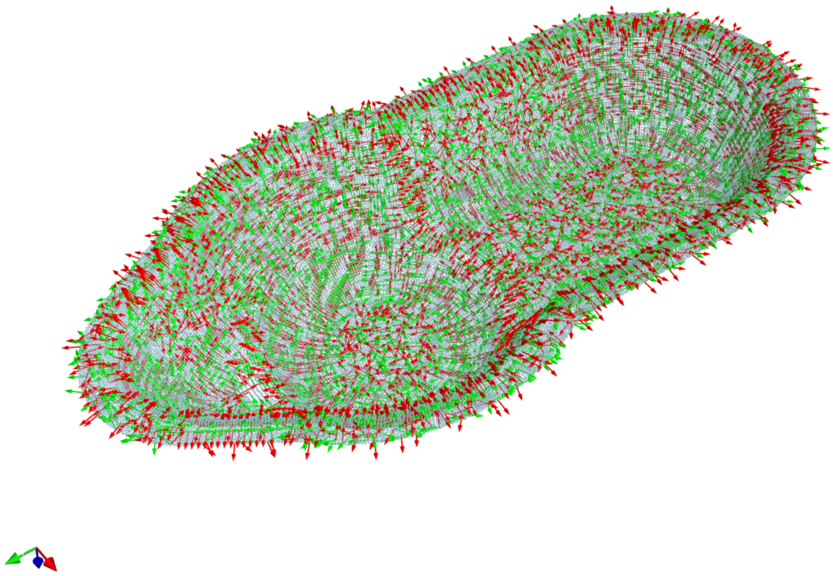

Figure 10: Estimated principal coordinates of the oil pan, numerical case. For clarity only every tenth principal coordinate system is visualized (red: α-direction, green: β-direction).

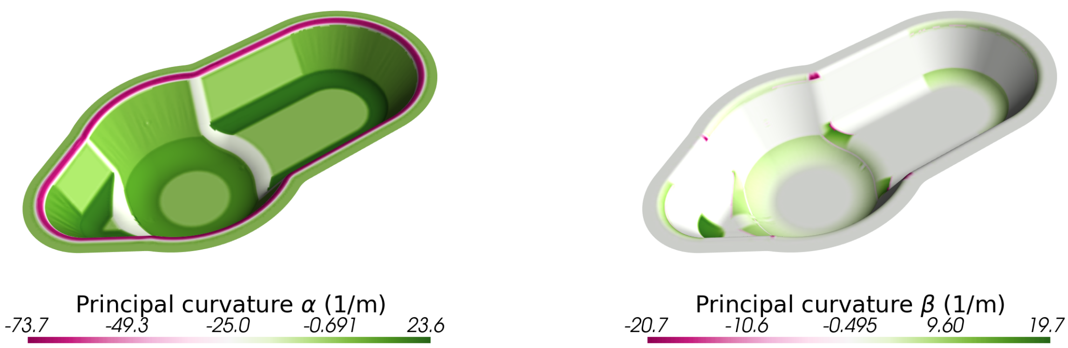

(a) First principal curvature.

(b) Second principal curvature.

Figure 11: Estimated principal curvatures of the oil pan, numerical case.

patterns in some regions. These are artifacts of the polynomial approximation, however, as the SI results below show, there is no substantial effect on the evaluated SI field.

Figure 12 shows the SI evaluation with polynomial filtering in comparison to an evaluation directly based on the forces and moments from the FE-simulation. Overall, there is a good agreement between the SI fields both qualitatively and quantitatively. From the source location, the main energy flow goes towards the rim of the component (area of the largest displacement) and circulates. Discrepancies between the FE-result and the proposed processing can be noted in areas of curvature discontinuities (e.g. at the rim or the bottom of the component). Since curvature discontinuities cannot be represented by the fitted polynomial the approximated quantities in these areas are smoothed out. As a result, the discrepancies enter the SI equations, eq. (2), and lead to unreasonably high SI amplitudes. However, the effect is reduced the smaller the curvature, which due to the constant discretization size is equivalent to a smaller local scale.

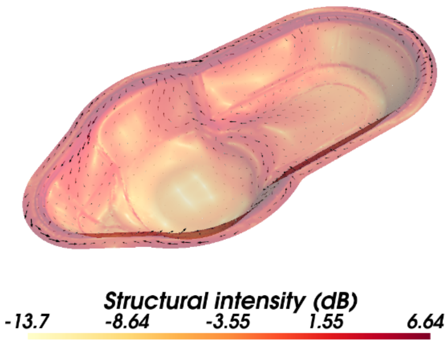

(a) Polynomial filtering.

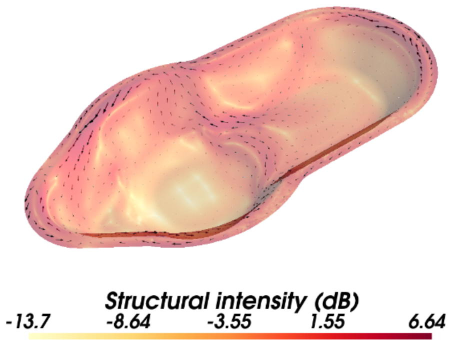

(b) Direct FE-evaluation.

Figure 12: Comparison of SI for the mockup oil pan, numerical case.

5.2 The effect of measurement noise

Three numerical test cases are evaluated to showcase the proposed approach under more realistic measurement conditions. Therefore, data from section 5.1 is used and noise is applied before the processing step. In the first case Gaussian noise with a standard deviation of 0.1 mm was applied to the geometry in the surface normal direction (cf. base case in section 4.1, see fig. 13a). In the second case, Gaussian noise is applied to the displacement field such that a nominal SNR of 44 dB is obtained. Since the noise is homogeneously applied to the whole component, regions with lower displacement amplitudes will be affected by a lower SNR, which is shown in fig. 13b. In the third case, both noise sources were included.

The result of the SI evaluation, fig. 13, shows significant impairment of the SI field for all three cases. Qualitatively, the impairment is greater if the noise is applied to the displacement field (or if both noise sources are present). The appearance of a noise floor can be observed, which is predominantly visible in regions of low SI magnitude. While the SI magnitude can hardly be used to deduct design decisions, the orientation of the vector field still is plausible except at the large curvature region of the rim.

The results indicate that a high accuracy of the geometry measurement, but predominantly a high SNR of the displacement field are required for a successful SI analysis. Further research is necessary to quantify the acceptable noise level and develop a suitable error metric for the comparison of the SI fields. In combination with the requirement of a sufficiently fine scale, this renders widely applicable SI measurements on curved plate-like structures with polynomial filtering a challenging endeavor.

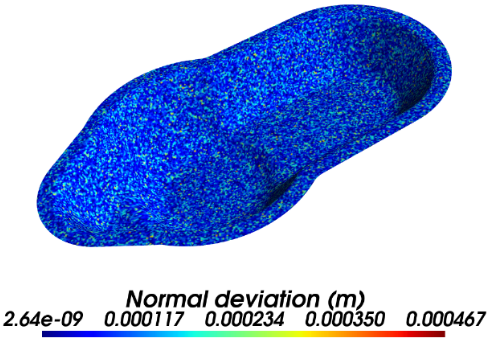

(a) Geometry deviation in surface-normal direction.

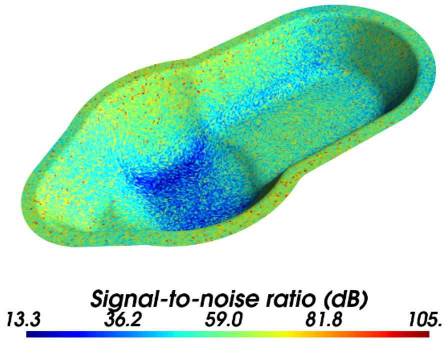

(b) SNR of the displacement field.

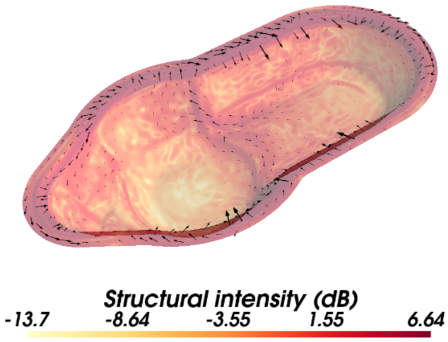

(c) SI evaluated based on noisy geometry.

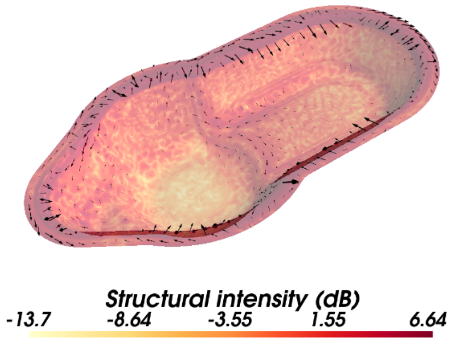

(d) SI evaluated based on noisy displacement field.

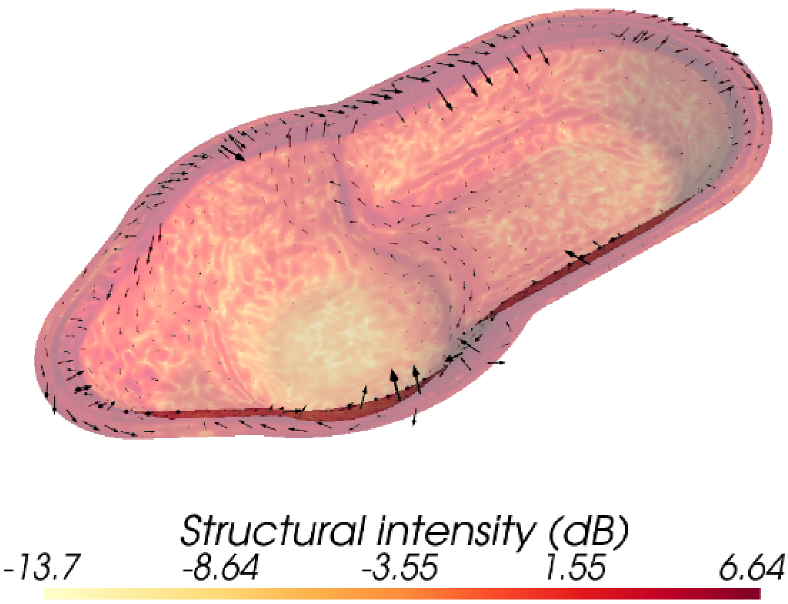

(e) SI evaluated based on noisy geometry and noisy displacement field.

Figure 13: Comparison of numerical SI under the influence of noise.

6 Experimental validation of the structural intensity analysis

Based on the results of the previous section, this section investigates camera-based SI analysis through polynomial filtering experimentally. First, the simplified case of a flat plate is considered, and second, the SI of the mockup oil pan as a curved plate-like structure is evaluated.

6.1 Structural intensity of a clamped, flat plate

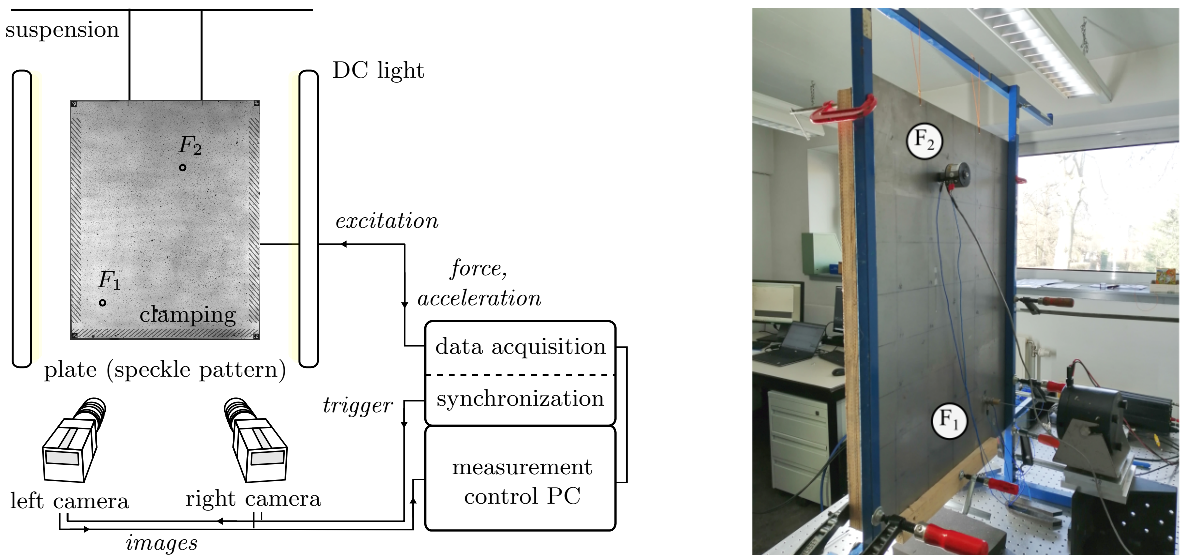

(a) Stereo camera setup. (b) Clamped plate with shaker excitation.

Figure 14: Flat plate experimental setup.

The SI flow through a rectangular, flat plate is considered. The plate has dimensions of 0.66 m by 0.86 m, thickness 1 mm and is made of steel with the homogeneous material parameters: Young's modulus of $210 \cdot 10^9$ Pa, density of 7893 kg/m^3, Poisson number of 0.3 and structural damping of 0.01. For the camera measurement, a speckle pattern is applied with spray paint (1 mm average speckle size). In the setup the plate is clamped along three edges and suspended by ropes at two points. The ropes restrain the vibration of the top edge, creating complex boundary conditions (see fig. 14). The excitation is applied in parallel with a stationary (F1) and an inertial shaker (F2). Depending on the phase relation of the shakers, the excitation frequency, and the deformation of the plate one of the shakers will inject energy into the system and the other one will remove energy out of the system. Two arbitrary frequencies were selected for the evaluation: 21.5 Hz (measured relative phase of the shakers: 0.39π) and 41.5 Hz (measured relative phase of the shakers: 0.52π).
A stereo camera system consisting of a *Ximea xiB-64 CB120CG-CM-X8G3* and a *JAI SP-12000-CXP4* camera is employed to measure the 3D displacement field (see fig. 14a). Both cameras operate on alike sensors with 12 Mpx resolution and 8 bit bit-depth. The maximum spatial resolution of 4096 x 3072 px with an average conversion factor of 3.98 px/mm (3.98 px per speckle) was selected. For this study a frame-rate of 100 fps was used and the displacement was evaluated with a window size of 25 px and on a uniform grid of 66x86 points leading to a discretization size of 0.01 m.
The measurement uncertainty was evaluated from a recording of the resting plate to approximately 1 µm. In accordance with the results of the numerical studies a slightly over-smoothing kernel radius of 7 times the discretization size is selected for the processing. First, principal coordinates and surface derivatives are obtained from polynomial filtering for geometry approximation, see fig. 15. The processing reveals that the plate is not perfectly flat but slightly curved with maximum curvature of 0.02. However, the curvature is sufficiently small to be practically neglected.

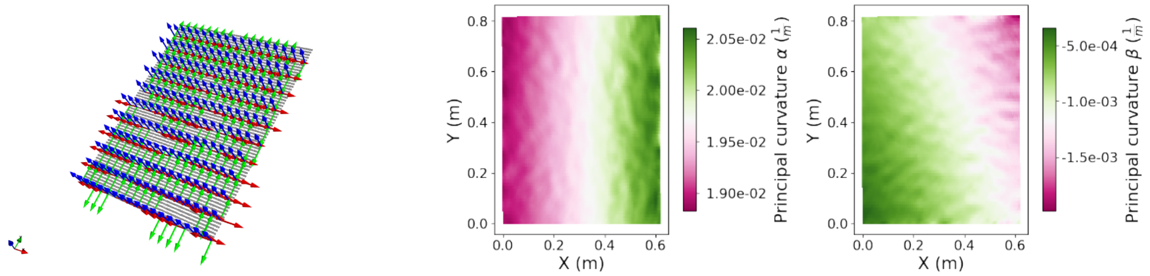

(a) Approximated principal coordinates. For clarity only every 30th principal coordinate system is visualized (red: α-direction, green: β-direction, blue: normal)

(b) Approximated curvature.

Figure 15: Geometry approximation of the flat plate.

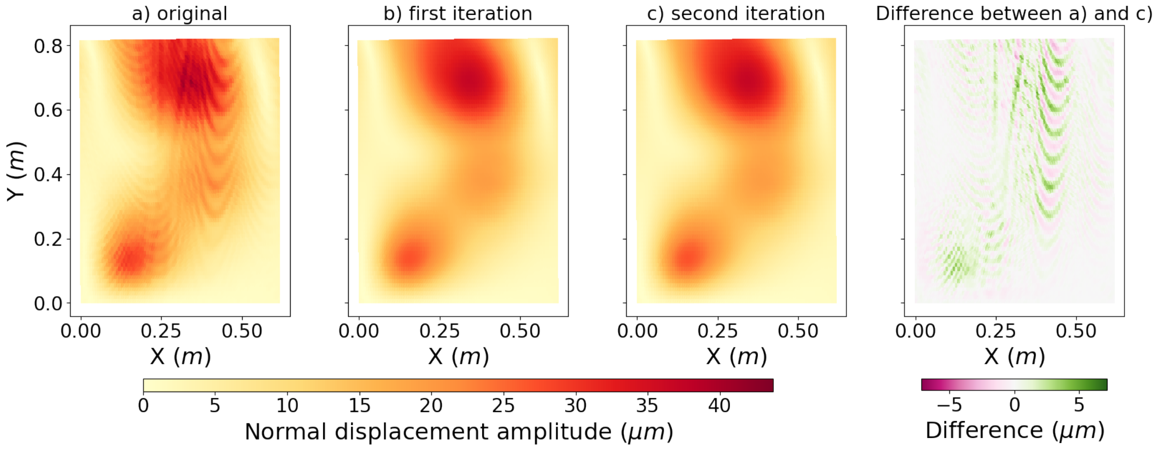

Figure 16: Normal displacement, original and smoothed fields at 21.5 Hz.

Next, the gradients of the displacement field are approximated by polynomial filtering with the same fitting radius. To reduce noise as well as artifacts originating from spatial aliasing of the optical flow method the processing was applied two times. The original normal displacement field, as well as the approximated versions are visualized in fig. 16 for 21.5 Hz. Aliasing is visible in the original displacement field in form of high-wavenumber fringe patterns but already after the first polynomial filtering iteration, this effect has vanished. While the amplitude of the normal displacement is in the range of 40 μm (SNR of 32 dB) both in-plane components are with 1 μm in the range of the measurement uncertainty and are therefore neglected in the further processing.

Finally, the SI field is evaluated. The results, along with a reference FE-simulation are depicted in fig. 17 for 21.5 Hz and 41.5 Hz. For the visualization of the vector field the arrows are clustered together for readability. In the FE-simulation, the boundary conditions of the plate were mimicked and the measured values of the shaker forces were applied as input. Similar to the oil pan in section 5, the FE-model of the plate consists of shell elements. It is discretized equivalently to the measurement, leading to 34 056 DOFs. Qualitatively and quantitatively the measured SI fields agree reasonably well with the FE-prediction. At 21.5 Hz the top shaker acts as an energy source and a direct transfer path to the bottom shaker, which acts as an energy sink, is visible. At 41.5 Hz the situation is reversed and the transfer path is influenced by vortices emerging at the top right and bottom left of the plate. While the FE-prediction shows no SI flow at the top border of the plate in the experiment small flows can be observed. These flows originate from the imperfect boundary conditions which could not be

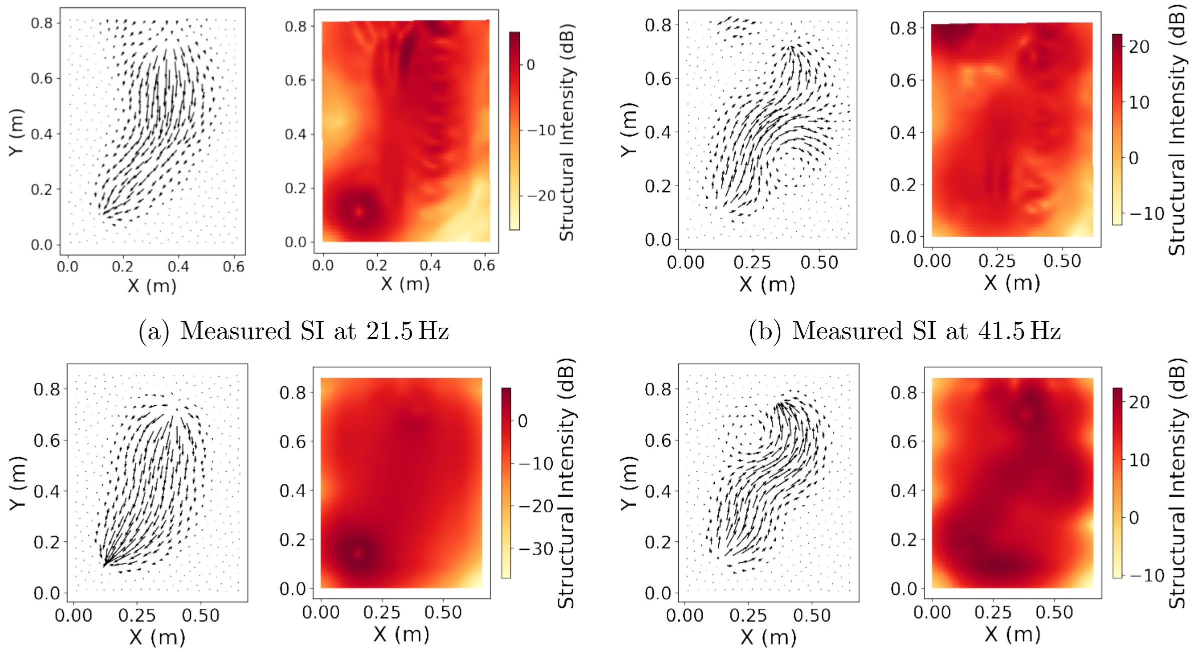

(a) Measured SI at 21.5 Hz

(b) Measured SI at 41.5 Hz

(c) Simulated SI at 21.5 Hz

(d) Simulated SI at 41.5 Hz

Figure 17: Comparison of measured and simulated SI. Each subfigure contains a visualization of the orientation of the SI vector (left) next to a plot of the magnitude of the SI field (right).

modeled in the FE-simulation. Also, due to the amplification through taking derivatives, there are still effects of the spatial aliasing visible in the experimental results.

6.2 Structural intensity of a freely suspended oil pan

An experimental SI analysis is conducted on the mockup oil pan component, which was introduced in section 5.1. Thereby, an equivalent camera measurement setup as for the flat plate in section 6.1 is used. The oil pan is suspended with two elastic cords to approximate free-free boundary conditions, see fig. 18a. A shaker, attached through a stinger, is used to excite the component as shown in fig. 18b. To increase the SNR, single frequency harmonic excitation is applied. As a measurement preparation, the inner side of the oil pan is coated with white spray paint in order to avoid reflections from the silver material and improve the contrast. In a second step, a speckle pattern is generated manually with a black marker, see fig. 18a. The speckle size is approximately 3 mm. The spatial resolution of the stereo camera system is set to 2016 x 1220 px with an average conversion factor of 1.9 px/mm (5.7 px per speckle). The spatial resolution is reduced compared to the nominal values of the cameras in favor of an increased frame- rate of 260 fps, which allowed to cover the first two eigenfrequencies of the system. The displacement field is evaluated with a window size of 25 px at 12 541 dense, evenly distributed points on the oil pan surface. Thereby, an average discretization size of 4.52 mm is obtained, leading to a maximum scale of $\gamma = 0.339$ (maximum curvature $|\kappa_1| = 75$).
For the processing, a fitting radius of 7 times the discretization size is used. Moreover, polynomial filtering was applied in three iterations to reduce the random error for each geometry and displacement processing. The resulting principal coordinates are visualized in fig. 19. Similar to the numerical case, the first principal direction is consistently oriented in the direction of the maximum curvature. In fig. 20, the main curved regions are clearly visible. However, overall the curvature is spatially smoothed due to the coarser discretization of the point cloud, the increased fitting radius and multiple iterations. The discontinuities in curvature in fig. 20a and fig. 20b can be explained by a change in the order of the magnitude of the principal curvatures.

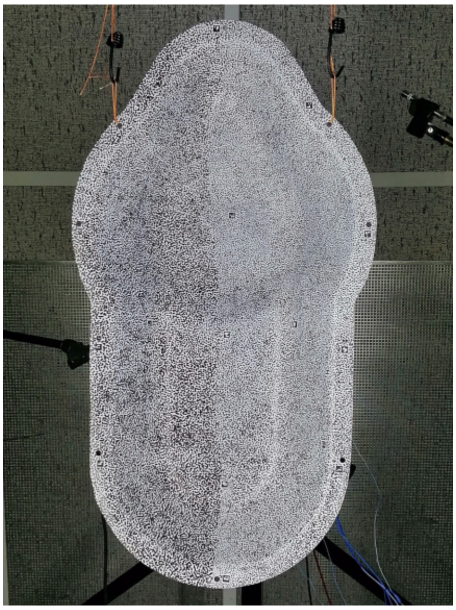

(a) Oil pan front side with speckle pattern.

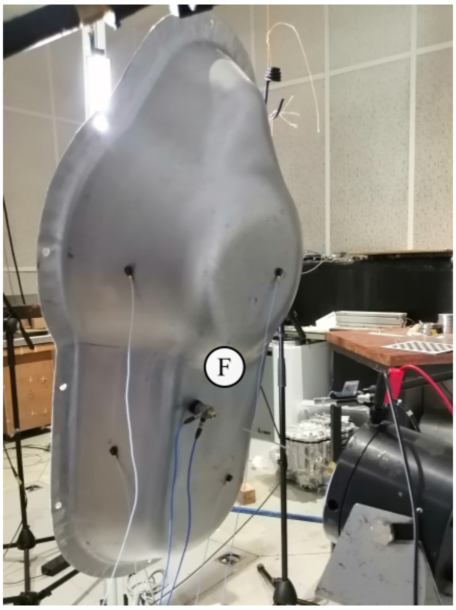

(b) Oil pan backside with shaker excitation.

Figure 18: Oil pan experimental setup.

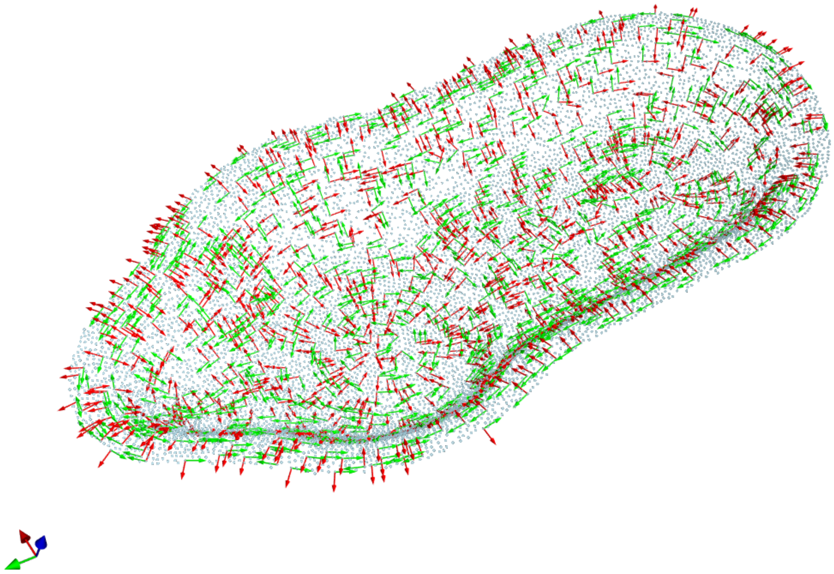

Figure 19: Estimated principal coordinates of the oil pan, experimental case. For clarity only every tenth principal coordinate system is visualized (red: α-direction, green: β-direction).

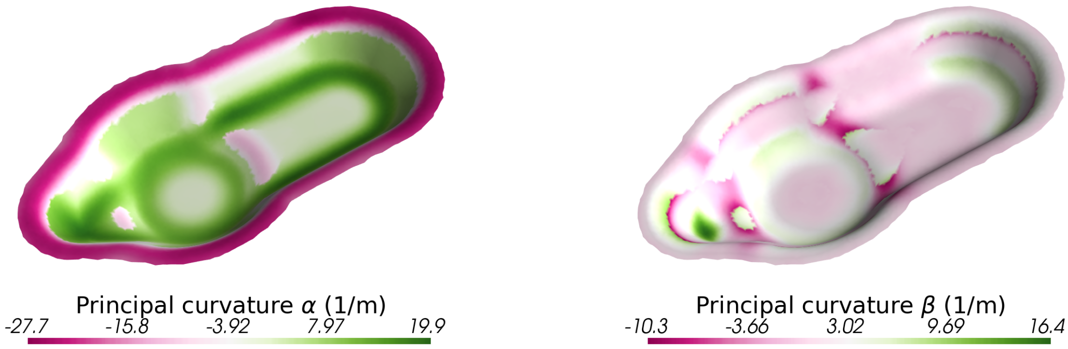

(a) First principal curvature. (b) Second principal curvature.

Figure 20: Estimated principal curvatures of the oil pan, experimental case.

In accordance with the previous numerical studies, the displacement field is evaluated at 105 Hz, close to the second eigenfrequency of the system. All three components of the global displacement field after polynomial filtering and their difference to the original measurement data is shown in fig. 21. The maximum amplitude of the vibration is 0.14 mm, predominantly oriented in global x- and z-direction. The measurement uncertainty is estimated from a recording of the resting structure, leading to a mean SNR of 43 dB, 46 dB and 32 dB for the x-, y-, and z-displacement component. Through the gradient approximation, a notable improvement in measurement quality can be observed. As the difference field in fig. 21 indicates, the z-direction is mostly affected by noise which is in accordance with the expectation of increased measurement uncertainty in the camera out-of-plane direction [4]. Also, the noise is increased in the inclined regions of the surface which were viewed by the camera at an angle. Locally, the difference reaches nearly 0.1 times amplitude of the displacement field.

Based on the complete smoothed displacement field and the approximated gradients, fig. 22a shows the resulting SI. It is observed that the highest SI magnitude is located at rim of the component where the displacements are largest. This is similar to the numerical study, fig. 12. There is a consistent SI flow to and away from the rim, however, the orientation pattern is clearly different from the numerical study and the location of the source is not visible.
Several influence factors could be responsible for the deviation from the numerical study: processing parameters, measurement noise and modeling assumptions.

Processing parameters As discussed for the geometry approximation in the experimental case, the selected polynomial filtering parameters, which were chosen to reduce measurement noise, resulted in bias. Both the estimated surface gradients and the estimated gradients of the displacement field are smoothed. This is due to the coarser discretization, the increased fitting radius and the use of more iterations as compared to the numerical study, see section 5.1. The minimum discretization size is imposed by the measurement and depends in the first place on the spatial resolution of the camera system. Clearly, the scale is with $\gamma = 0.339$ not sufficiently small to resolve the curved areas accurately (the scale in the numerical case was $\gamma = 0.225$ and in the cylinder base case $\gamma = 0.08$).

Measurement noise Even though polynomial filtering reduces the measurement noise, the numerical differentiation is still amplifying the uncertainty. Therefore , the noise propagation through the required spatial gradients can have a severe effect on the evaluated SI. While filtering is one aspect for noise reduction, the source lies in the accuracy of the measurement system. Especially, the inclined regions of the oil pan, where increased noise was observed, show an unreasonably high SI amplitude. the influence of measurement noise also depends on the vibration amplitude, which is problem-dependent.

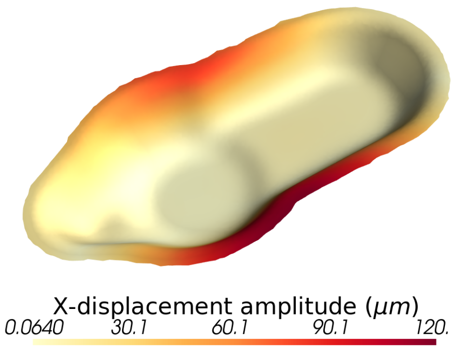

(a) Noise-reduced X-displacement.

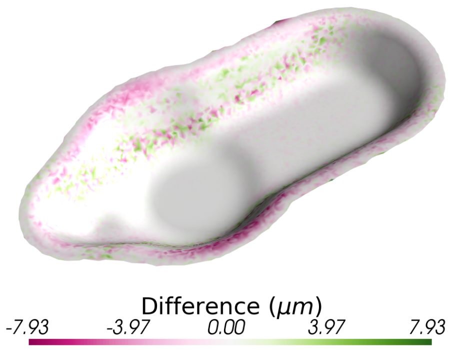

(b) Difference of noise-reduced and raw X-displacement.

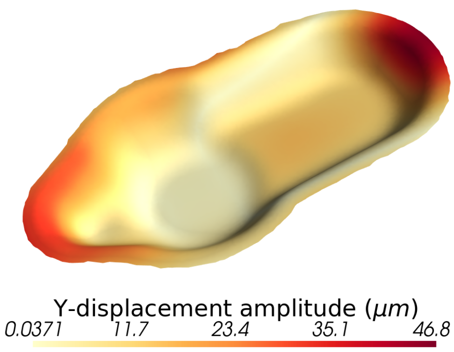

(c) Noise-reduced Y-displacement.

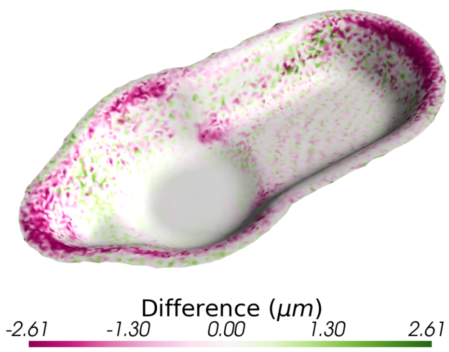

(d) Difference of noise-reduced and raw Y-displacement.

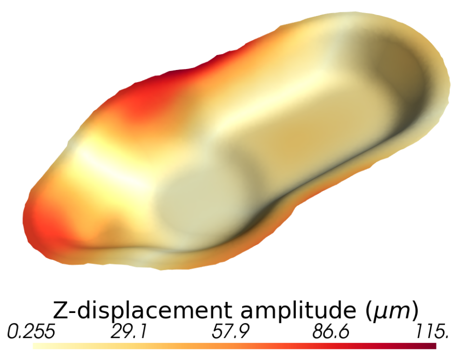

(e) Noise-reduced Z-displacement.

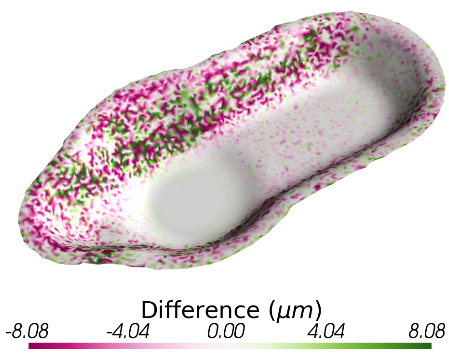

(f) Difference of noise-reduced and raw Z-displacement.

Figure 21: Displacement field of the oil pan field at 105 Hz.

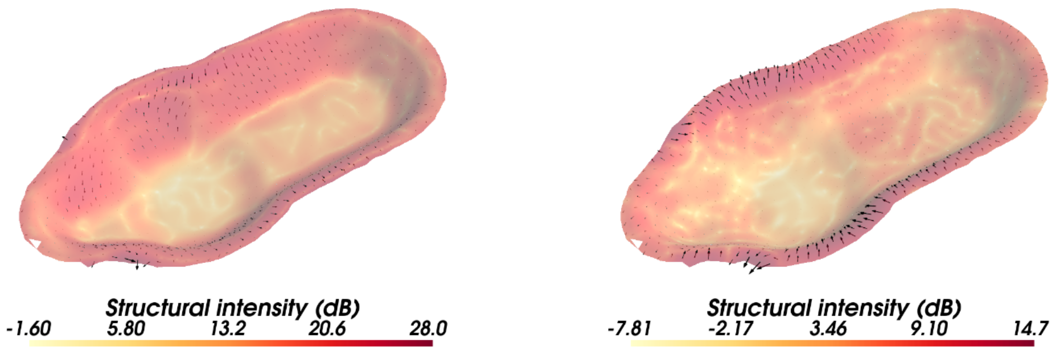

(a) Complete SI field.

(b) SI without the local in-plane displacement components.

Figure 22: Experimental SI analysis.

Modeling assumptions Another reason for the deviation of the experimental SI field from the numerical results could be that the assumption of homogeneous material properties is invalid. It is well-known that deep-drawn components like the mockup oil pan are subject to local hardening and thickness variations [5]. Specifically, for the mockup oil pan it was shown that an updated patch-wise distribution of thickness and Young's modulus significantly improves the match between FE-simulations and reference measurements [28]. In the present paper, homogeneous material parameters were assumed as a simplification to avoid incorporating spatial derivatives of the material parameter distribution in the SI computation. Moreover, in practice for a SI analysis on an unknown component it is difficult to determine the material parameter distribution experimentally.

In contrast to evaluating the full SI field, neglecting the local in-plane displacement components (i.e. neglecting the normal and in-plane shear forces) reveals the source location, see fig. 22b. A possible reason is that the local in-plane displacement components are much smaller than the out-of-plane component and therefore more susceptible to noise. This renders the evaluation of the normal forces more difficult than the moments and transverse shear forces.

7 Conclusion

In the present paper, a mesh-free, polynomial filtering approach for the computation of structural intensity based on camera measurements for curved surfaces is proposed. The approach consists of a geometry and a gradient approximation step and relies on the Kirchhoff-Love plate theory. From numerical studies, it was shown that the optimal processing parameters, spatial discretization and fitting radius are dependent on the amount of noise in the measurement. A scale was introduced to apply the results independent of the curvature. Furthermore, the approach can be used in multiple iterations as a smoothing filter for the geometry as well as for the displacement field.

Polynomial filtering was validated experimentally in the case of a flat plate under shaker excitation and the results agree well with reference finite element simulations. Source, sink, and energy transfer paths could be identified at the two analyzed frequencies.

For generalization to curved surfaces, numerical and experimental studies on a mockup oil pan component under point force excitation were conducted. In the numerical case, valid results were obtained when no noise was applied. Through the introduction of noise on the geometry or the displacement field, impairment of the structural intensity field was observed. Nevertheless, it was shown that qualitative indications remain possible. An experimental campaign on the mockup oil pan produced realistic displacement fields and the smoothing abilities of the proposed approach could be demonstrated. However, the resulting structural intensity field is difficult to interpret and both, measurement noise and material inhomogeneities lead to a deviation from the numerical results.

The present paper presents an initial study on the development of a "structural intensity camera" for observation of the structural intensity flow in an equivalent manner as an acoustic camera allows the localization of acoustic sources. Several challenges remain to be solved in future research to realize such a device for general industrial components: sufficient signal-to-noise ratio (technological improvement, advanced noise reduction), treatment of inhomogeneous material properties or thickness, transition to time domain structural intensity analysis, and real-time capable processing algorithms.

8 CRediT authorship contribution statement

Felix Simeon Egner: Conceptualization, Methodology, Software, Investigation, Writing - Original Draft. Luca Sangiuliano: Conceptualization, Methodology, Writing - Review & Editing. Régis Fabien Boukadia: Methodology, Writing - Review & Editing. Sjoerd van Ophem: Conceptualization, Supervision, Methodology, Writing - Review & Editing. Wim Desmet: Conceptualization, Supervision. Elke Deckers: Conceptualization, Supervision, Methodology, Writing - Review & Editing.

9 Declaration of competing interest

The authors declare that they have no known competing financial interests or personal relationships that could have appeared to influence the work reported in this paper.

10 Acknowledgments

Internal Funds KU Leuven and the Research Foundation – Flanders (FWO), grant no. G095120N are gratefully acknowledged for their support. Furthermore, the research of S. van Ophem (fellowship no. 1277021N) is funded by a grant from the Research Foundation - Flanders (FWO).

References

[1] H. Al Ba'ba'a, M. A. Attarzadeh, and M. Nouh. "Experimental Evaluation of Structural Intensity in Two-Dimensional Plate-Type Locally Resonant Elastic Metamaterials". In: *Journal of Applied Mechanics* 85.4 (2018), p. 041005. ISSN: 0021-8936, 1528-9036. DOI: 10.1115/1.4039042.

[2] J. R. F. Arruda and P. Mas. "Predicting and Measuring Flexural Power Flow in Plates". In: Second International Conference on Vibration Measurements by Laser Techniques: Advances and Applications. Ed. by E. P. Tomasini. Ancona, Italy, 1996, pp. 149–163. DOI: 10.1117/12.248634.

[3] S. Avril et al. "Comparison of Two Approaches for Differentiating Full-Field Data in Solid Mechanics". In: *Measurement Science and Technology* 21.1 (2010), p. 015703. ISSN: 0957-0233, 1361-6501. DOI: 10.1088/0957-0233/21/1/015703.

[4] R. Balcaen et al. "Stereo-DIC Uncertainty Quantification Based on Simulated Images". In: *Experimental Mechanics* 57.6 (6 2017), pp. 939–951. ISSN: 0014-4851, 1741-2765. DOI: 10.1007/s11340-017-0288-9.

[5] V. K. Balla. "Process Parameter, Geometric & Vibro-Acoustic Variability: The Study of Causation in the Deep Drawing Process". PhD thesis. KU Leuven, 2022.

[6] J. D. Blotter, R. L. West, and S. D. Sommerfeldt. "Spatially Continuous Power Flow Using a Scanning Laser Doppler Vibrometer". In: *Journal of Vibration and Acoustics* 124.4 (2002), pp. 476–482. ISSN: 1048-9002, 1528-8927. DOI: 10.1115/1.1497363.

[7] T. Eck and S. Walsh. "Measurement of Vibrational Energy Flow in a Plate with High Energy Flow Boundary Crossing Using Electronic Speckle Pattern Interferometry". In: *Applied Acoustics* 73.9 (2012), pp. 936–951. ISSN: 0003682X. DOI: 10.1016/j.apacoust.2012.04.002.

[8] F. S. Egner et al. "High-Speed Camera Based Experimental Modal Analysis for Dynamic Testing of an Automotive Coil Spring". In: *SAE International Journal of Advances and Current Practices in Mobility* 4.1 (2021). ISSN: 2641-9637. DOI: 10.4271/2021-01-1119.

[9] S. Fleishman. "Point Set Surfaces". PhD thesis. Tel-Aviv University, 2003.

[10] T. Hering. "Strukturintensitätsanalyse als Werkzeug der Maschinenakustik". PhD thesis. TU Darmstadt, 2012.

[11] N. Kleinfeller, J. Bös, and T. Melz. "Measurement of the Structural Intensity of Curved Shell Structures by Means of 3D Laser Vibrometry". In: 23rd International Congress on Acoustics. Aachen, Germany: European Acoustics Association, 2019.

[12] J. Liu, Y. Liu, and J. S. Bolton. "The Application of Acoustic Radiation Modes to Engine Oil Pan Design". In: SAE Noise and Vibration Conference and Exhibition. SAE, 2017, pp. 2017-01–1844. DOI: 10.4271/2017-01-1844.

[13] D. U. Noiseux. "Measurement of Power Flow in Uniform Beams and Plates". In: *The Journal of the Acoustical Society of America* 47 (1B 1970), pp. 238–247. ISSN: 0001-4966. DOI: 10.1121/1.1911472.

[14] D. Panozzo, E. Puppo, and L. Rocca. "Efficient Multi-scale Curvature and Crease Estimation". In: 2nd International Workshop on Computer Graphics, Computer Vision and Mathematics, GraVisMa 2010. Brno, Czech Republic, 2010, pp. 9–16.

[15] J.-C. Pascal, J.-F. Li, and X. Carniel. "Wavenumber Processing Techniques to Determine Structural Intensity and Its Divergence from Optical Measurements without Leakage Effects". In: *Shock and Vibration* 9.4-5 (2002), pp. 57–66.

[16] G. Pavić. "Structural Surface Intensity: An Alternative Appraoch in Vibration Analysis and Diagnosis". In: *Journal of Sound and Vibration* 115.3 (1987), pp. 405–422. DOI: 10.1016/0022-460X(87)90286-0.

[17] G. Pavić. "Structure-Borne Energy Flow". In: *Handbook of Noise and Vibration Control*. Ed. by M. J. Crocker. Hoboken, N.J: John Wiley, 2007. ISBN: 978-0-471-39599-7.

[18] G. Petrone et al. "Numerical and Experimental Investigations on Structural Intensity in Plates". In: *Composite Structures* 140 (2016), pp. 94–105. ISSN: 02638223. DOI: 10.1016/j.compstruct.2015.12.034.

[19] F. Pires, S. Vanlanduit, and J. J. J. Dirckx. "Structural Intensity Analysis on Irregular Shells". In: *Journal of Vibration and Acoustics* 141.1 (2019), p. 011011. ISSN: 1048-9002, 1528-8927. DOI: 10.1115/1.4040926.

[20] F. Pires et al. "Structural Intensity Analysis of Flat Plates Based on Digital Stroboscopic Holography Measurements". In: *Journal of Sound and Vibration* 428 (2018), pp. 168–178. ISSN: 0022460X. DOI: 10.1016/j.jsv.2018.05.010.

[21] F. Pires et al. "Structural Intensity Assessment on Shells via a Finite Element Approximation". In: *The Journal of the Acoustical Society of America* 145.1 (2019), pp. 312–326. ISSN: 0001-4966. DOI: 10.1121/1.5087564.

[22] N. B. Roozen, J. Guyader, and C. Glorieux. "Measurement-Based Determination of the Irrotational Part of the Structural Intensity by Means of Test Functional Series Expansion". In: *Journal of Sound and Vibration* 356 (2015), pp. 168–180. ISSN: 0022460X. DOI: 10.1016/j.jsv.2015.06.040.

[23] K. Saijyou and S. Yoshikawa. "Structural Intensity Measurement of Cylindrical Shell Based NAH Technique and Influences of a Rib on the Acoustic Energy Flow". In: *Journal of the Acoustical Society of Japan* 20.2 (1999), pp. 125–136.

[24] A. Savitzky and M. J. E. Golay. "Smoothing and Differentiation of Data by Simplified Least Squares Procedures." In: *Analytical Chemistry* 36.8 (1964), pp. 1627–1639. ISSN: 0003-2700. DOI: 10.1021/ac60214a047.

[25] M. R. Shepherd et al. "Structural Intensity Modeling and Simulations for Damage Detection". In: *Journal of Vibration and Acoustics* 134.5 (2012), p. 051004. ISSN: 1048-9002, 1528-8927. DOI: 10.1115/1.4006376.

[26] A. Spek, W. H. Li, and T. Drummond. *A Fast Method For Computing Principal Curvatures From Range Images.* Version 2. 2017.

[27] N. Tanaka et al. "Vortex Structural Power Flow in a Thin Plate and the Influence on the Acoustic Field". In: *The Journal of the Acoustical Society of America* 96.3 (1994), pp. 1563–1574. ISSN: 0001-4966. DOI: 10.1121/1.410235.

[28] S. van Ophem, E. Deckers, and W. Desmet. "Model Based Virtual Intensity Measurements for Exterior Vibro-Acoustic Radiation". In: *Mechanical Systems and Signal Processing* 134 (2019), p. 106315. ISSN: 08883270. DOI: 10.1016/j.ymssp.2019.106315.

[29] E. Ventsel and T. Krauthammer. *Thin Plates and Shells - Theory, Analysis and Applications.* 2001. 688 pp. ISBN: 978-0-429-22131-6.

[30] C. Wang et al. "On the Application of B-spline Approximation in Structural Intensity Measurement". In: *Journal of Sound and Vibration* 290.1-2 (2006), pp. 508–518. ISSN: 0022460X. DOI: 10.1016/j.jsv.2005.04.011.

[31] S. Wildy. "Scanning Laser Doppler Vibrometry for Strain Measurement and Damage Detection". PhD thesis. University of Adelaide, 2012.

[32] R. Winter, S. Heyen, and J. Biedermann. "Experimental Structure Intensity Analysis of an Airbus A400M Fuselage Structure Using High-Resolution Vibration Measurements". In: *Proceedings of DAGA 2019.* DAGA. German Acoustical Society, 2019.